REVIEWS OF TOPICAL PROBLEMS

Mass ejections from the solar atmosphere

Physics – Uspekhi **62** (9) 847 – 864 (2019)

REVIEWS OF TOPICAL PROBLEMS PACS numbers: **52.30. – q**, **96.60. – j**, 96.60.Hv, 96.60.P – , 96.60.Q –

Mass ejections from the solar atmosphere

B P Filippov

DOI: https://doi.org/10.3367/UFNe.2018.10.038467

Contents

Abstract. Coronal mass ejections are the largest-scale eruptive phenomenon in the solar system. Their drastic effect on space weather is a reason for the significant interest in observing, simulating, and forecasting these events. We describe the main features of mass ejections from the solar atmosphere, their physical parameters and frequency, and its dependence on the solar cycle phase. We consider potential sources of ejections in the solar atmosphere and magnetic field configurations wherein the energy needed for sudden explosive acceleration of large masses of matter can be stored. The main instabilities of coronal structures that lead to the triggering and development of eruptive processes are analyzed. We show that coronal mass ejections are related to other manifestations of solar activity, while the eruptive processes observed using various techniques in various layer of the solar atmosphere and interplanetary space are the same phenomenon. We discuss indicators of the Sun's pre-eruptive regions approaching a catastrophe and the options to use them to forecast eruptions and space weather disturbances.

Keywords: coronal mass ejections, prominences, filaments, magnetic fields

1. Introduction

The total energy flux emitted by the Sun into its environment has a spectacular and comforting invariability. The Sun's radiating surface, the photosphere, is almost an ideal sphere. Variations in the photosphere diameter recorded in various years are less than 10^{-5}, hardly over the accuracy of existing methods of measurement. The energy flux from the Sun at a distance of one astronomic unit (the average distance between the Sun and Earth) is 1366 W m^{-2}. Although spots — areas with reduced brightness — sporadically appear in the photosphere, the radiation missing due to their emergence is always compensated, and with some excess, by the enhanced brightness of solar flares, the bright areas that always accompany the spots. Precise measurements of the integral flux of solar radiation that have been conducted by spacecraft outside Earth's atmosphere for almost four decades reveal short-time (several-day-long) variations within 0.4% and systematic increases and decreases by less than 0.1% related to the epochs of solar activity maxima and minima [1].

Such invariability is not observed in the entire spectral range, however. The shortwave segment of the solar radiation spectrum, being absorbed by Earth's atmosphere, has only become available for study after the birth of extraterrestrial astronomy. When viewed in the ultraviolet (UV) and X-ray ranges, the Sun turns out to be a strongly variable star. The radiation flux in the near-UV range varies greatly during the solar activity cycle ($\sim$ 11 years), while the variation factor in the extreme UV and soft X-ray ranges can be as large as tens or hundreds [2, 3]. Radiation at the other end of the spectrum, in the radio wave range, is also variable and exhibits periodic changes. The total radio wave radiation flux changes synchronously with the Wolf number, a quantity that characterizes the number of sunspots visible on the Sun's surface [4]. The radio wave radiation flux at a wavelength of 10.7 cm is a parameter that can characterize solar activity for many applied problems related to the assessment and forecast of the state of Earth's magnetosphere better than discrete Wolf numbers. The intensity of the Sun's radio wave radiation can increase during solar flares by several orders of magnitude [5].

The most intense and sharp increases of shortwave radiation occur during solar flares, sporadic nonstationary events in the Sun's atmosphere. Hard X-ray and gamma-ray

B P Filippov Pushkov Institute of Terrestrial Magnetism, the Ionosphere and Radio Wave Propagation, Russian Academy of Sciences, Kaluzhskoe shosse 4, 108840 Troitsk, Moscow, Russian Federation
E-mail: bfilip@izmiran.ru

Received 17 May 2018, revised 16 October 2018
Uspekhi Fizicheskikh Nauk **189** (9) 905 – 924 (2019)
DOI: https://doi.org/10.3367/UFNr.2018.10.038467
Translated by M Zh Shmatikov; edited by A M Semikhatov

radiation is detected during strong flares. The strongest flares also manifest themselves in a short-duration surge of brightness of small photosphere areas. It is owing to this phenomenon that solar flares were discovered in 1859 by two British astronomers, Carrington and Hodgson, who independently observed [6, 7] the by now strongest flare on September 1, 1859. A geomagnetic storm began seventeen hours later on Earth, this coincidence prompting a guess that terrestrial electromagnetic perturbations are related to events on the Sun, although Carrington at the November session of the Royal Astronomical Society urged not to make hasty conclusions, stressing that "one swallow does not a summer make" [6].

After the invention of the spectrohelioscope and the spectroheliograph, which enabled observing the Sun in narrow spectral lines, in particular, in the hydrogen Balmer line Hα, it turned out that flares occur on the Sun rather frequently; however, not all of them are visible in white light (continuum). Also, prominences — bright features extending outward from the chromosphere at the solar disk edge — became observable in the spectral lines characteristic of chromosphere radiation. The prominences could only be observed earlier during total solar eclipses, and for a long time there had been no common opinion about whether these objects were related to the Sun or the Moon. Regular observations of prominences showed that some of them abruptly start elevating above the surface and are gradually accelerated. The velocity of some elevating (eruptive) prominences is higher than the escape velocity from the Sun's gravitational field (~ 600 km s^{-1}); however, it was not possible to trace whether they actually leave the Sun, because their brightness gradually decreases to become comparable, at a distance of the order of the Sun's radius, to the background created by light scattered by Earth's atmosphere.

Although it was hypothesized immediately after the discovery of flares that during a flare the Sun emits rapidly moving particles that reach Earth one to four days later and trigger geomagnetic perturbations, it was not possible to obtain direct confirmation of this hypothesis for a hundred years. As knowledge about the properties of the solar atmosphere and, in particular, pieces of evidence that the temperature of its outer layers, the corona, is very high (more than 1 MK) have been accumulating, a theoretical assumption has taken shape that there is a continuous stationary outflow of matter from the solar atmosphere into the interplanetary medium, referred to as the 'solar wind' [8].

Deviation of comet tails in the direction away from the Sun has been considered for a long time to be indirect evidence of the existence of a continuous flow of particles moving away from the Sun [9]. Solar wind particles were directly detected by the first interplanetary spacecraft Luna-1, Luna-2, and Mariner-2 [10, 11]. Because long-lived solar-wind sources rotate with the Sun with a period of about 27 days, flows of particles with specific properties (fast solar wind) appear in the vicinity of Earth with the same periodicity, causing recurrent geomagnetic perturbations.

The fast solar wind is now known to outflow from coronal holes, the areas dominated by the magnetic field whose field lines extend to interplanetary space. The coronal holes near heliographic poles exist for several years in minimum activity periods. The lifetime of low-latitude coronal holes can infrequently be as long as many revolutions of the Sun. Explorations of the properties of solar wind conducted by many spacecraft have shown that it is a nonstationary and turbulent phenomenon. Apart from the presence of two types of wind — a fast wind whose velocity is 700–800 km s^{-1} and a slow one whose velocity is 400–450 km s^{-1} — and two dominant directions of the magnetic fields — towards the Sun and away from it — relatively short-term variations in parameters are observed. These variations are related to the passage of compact formations, some of which are referred to as interplanetary magnetic clouds due to characteristic properties of the magnetic field.

The solar corona becomes visible to the naked eye and explorable from Earth's surface only during short moments of solar eclipse totality. The continuous radiation of the photosphere that is scattered by the coronal matter and whose brightness is 10^6 times larger than the corona brightness can be detected at a distance of several Sun radiuses. In 1930, Bernard Lyot, a French astronomer and optician, designed a telescope, named a coronagraph, in which he used a 'man-made Moon' to eclipse the light coming from the photosphere [12]. Despite special measures taken to remove scattered light from the device, it was virtually impossible to obtain images of the 'white corona' in terrestrial conditions due to scattering of photosphere radiation in Earth's atmosphere. However, coronagraphs proved to be very effective in very narrow spectral regions that contain emission spectral lines of the corona, owing to which they are still in use in some observatories.

Lyot's idea could only be implemented in its entirety when extraterrestrial astronomy emerged [13]. On December 14, 1971, one of the first coronagraphs launched beyond the atmosphere aboard OSO-7 (Orbiting Solar Observatory 7), a US satellite, discovered a bright structure on the corona image moving with a velocity greater than 1,000 km s^{-1}. Similar phenomena have been copiously observed and explored in detail since then using other orbital coronagraphs. It became clear that the observed motion of bright structures is not a wave phenomenon but real motion of matter, which was named coronal mass ejection (CME). An array of three coronagraphs operated by the Solar and Helioscopic Observatory (SOHO) enables tracking the motion of ejected matter to distances as long as 30 solar radiuses ($R_\odot$), while two special cameras of the Solar Terrestrial Relations Observatory (STEREO) can track matter ejected from the corona as far as Earth's orbit. Owing to observations made by STEREO, which is located away from the Sun–Earth line, perturbations of solar wind parameters measured by the Advanced Composition Explorer (ACE) and Wind satellites are now unambiguously related to the arrival of CMEs [14].

Spacecraft equipped with various plasma detectors record the arrival of CMEs on the basis of rapid variations in interplanetary medium parameters. Such perturbations originating in the Sun are referred to as interplanetary CMEs (ICMEs) [15]. They are identified by an increase in the interplanetary magnetic field (from ~ 5 nT in a quiescent state to several tens of nT) and a smooth change in its direction, a decrease in the proton temperature, the ratio of gas and magnetic pressures, and the plasma β, and a number of other indicators [16]. Measurements made at a single point (in situ) apparently only yield a time profile of how quantities change; but if the velocity of passage of the perturbation is known, an attempt can be made to reconstruct its spatial structure as well.

For example, a family can be distinguished among all detected interplanetary ejections that has the most regular

structure. When such a mass ejection passes by, the magnetic field vector smoothly deviates at the point of measurement by more than 30° while preserving a predominant preferred direction. These perturbations are referred to as magnetic clouds. The magnetic field in the clouds, which is reconstructed using the measurements made when the CME passes by a space probe, is structured as embedded coaxial cylindrical magnetic surfaces wherein the pitch angle of field lines increases as the distance from the axis grows [17]. Such configurations are referred to as magnetic flux ropes. The fraction of magnetic clouds in the total number of ICMEs depends on the solar cycle phase and ranges from $\sim 30\%$ in the maximum to more than 80% in the minimum [18].

Plasma with a trapped magnetic field that is ejected with a large velocity from the corona apparently keeps moving in the interplanetary space, gradually transforming into an interplanetary magnetic cloud incorporated into the solar wind flow. If the initial velocity of the cloud is larger than that of the ambient solar wind, the cloud is decelerated by the wind; otherwise, it is accelerated. The giant inhomogeneity moving in the heliosphere affects the passage of radio waves and propagation of galactic and solar cosmic rays. A collision of the magnetic cloud with Earth's magnetosphere causes a geomagnetic storm that heavily impacts engineering activities of humans and their health. As soon as this connection became clear, interest in coronal processes, which was earlier of a pure exploratory nature, changed to a more practical one. Flares that had earlier been considered to be the primary geoeffective agent were pushed away to the background. Their importance for geophysics has even been declared 'a myth' [19]. Due to the importance of the studies of CMEs for the 'space weather' problem, interest in these problems remains strong. A large number of studies in which the origins, development, and effect of CMEs on the heliosphere were explored have been reflected in a number of monographs and reviews published during the last decade [20–26].

We here review the main properties of mass ejections from the solar atmosphere to the interplanetary space, the state of the Sun's areas from which they originate, the reasons for and triggers of eruptive phenomena, and options for forecasting these phenomena.

2. Methods and instruments for observing dynamic processes in the solar atmosphere and interplanetary space

The optical density of the solar atmosphere in the continuous spectrum is extremely small; therefore, a standard telescope without any enhancements only enables observing the photosphere with the granulation intrinsic to it and (in years of enhanced activity) sunspots and faculae. But because atoms and ions of the rarified atmosphere absorb and emit light in certain spectral lines, the optical density of various atmospheric layers in narrow spectral bands of these lines becomes sufficient for detecting their emission or absorption.

Spectroscopic methods for studying the Sun are very fruitful and helpful because they provide information about the physical quantities in the radiation area: density, temperature, velocity, and magnetic field. However, to study the motion of matter in the solar atmosphere, 2D distributions are needed. By scanning the spectrograph slit across the solar disk or using a monochromatic filter, an image of the Sun can be obtained in the selected line. The Hα Balmer-series hydrogen line is most widely used in terrestrial observations of the Sun. The fine structure of the chromosphere and prominences above the limb of the Sun are well seen in the light of this line. If projected onto the disk, the prominences are observed as narrow dark strips, solar filaments.

The advantage of a spectroheliograph that scans the spectrograph slit is that any line or line segment can be used without restrictions; however, some time is needed to obtain an image. This instrument is more suitable for exploring stationary or slowly varying objects. Filter-based observations made with a high recording frequency enable detecting fast phenomena that develop during flares or eruptions. Observatories that monitor the entire disk of the Sun are located in various time zones to create favorable conditions for continuous observations; however, this is not always possible due to weather conditions. Some observatories are united into grids combining identical or similar instruments: Global High-Resolution Hα Network and Synoptic Optical Long-term Investigations of the Sun (SOLIS).

The solar corona heated to a temperature of ~ 1 MK radiates in the lines that belong to the ultraviolet and X-ray ranges to which Earth's atmosphere is not transparent. Telescopes intended for observations at these wavelengths must be located outside the atmosphere onboard a spacecraft. The photosphere barely radiates in the UV and X-ray ranges; therefore, for the corona to be observable in these lines, it is not necessary to eclipse the solar disk.

The spatial and time resolution of space telescopes increases with each new space mission. The Japanese satellites Yohkoh and Hinode were successful in conducting observations in the soft X-ray range. The corona radiation in UV lines is observed by telescopes aboard the SOHO, STEREO, PROBA2 (PRoject for OnBoard Astronomy), and SDO (Solar Dynamic Observatory) space observatories. Ultraviolet telescopes have also been installed on the Russian satellites KORONAS-I, KORONAS-F, and KORONAS-Foton. The emission corona brightness, which is proportional to the density of radiating particles squared, decreases with distance faster than the brightness of the scattering white corona, which is proportional to the first power of the density. The field of view of space UV telescopes is therefore usually restricted by distances (1.5–1.8) $R_\odot$. They can be used within such distances (measured from the disk center) to observe the motion of eruptive prominences, coronal loops, and coronal jets.

The field of view of coronagraphs that detect the photosphere radiation scattered by free electrons is, on the contrary, conceptually limited from below, because the entire photosphere should be eclipsed with an occulting disk. Diffraction on this disk limits the minimum distance from the limb at which the coronal radiation can be observed. To span a large range of radial distances, a task of importance for exploring CMEs, several coronagraphs with various dimensions of the occulting disks and fields of vision are deployed. The LASCO (Large Angle Spectroscopic Coronagraph) array of coronagraphs aboard STEREO consists of three instruments whose fields of vision are (1.1–3) $R_\odot$, (1.5–6) $R_\odot$, and (3.7–30) $R_\odot$ [27]. Two coronagraphs aboard the STEREO observatory have fields of vision (1.5–4) $R_\odot$ and (2.5–15) $R_\odot$ [28].

To detect CMEs at larger distances from the Sun, special cameras (heliosphere imagers) are employed. Because their optical axes are aligned in a direction somewhat away from the Sun, the photosphere light does not get into the objective lenses. However, to prevent scattering on the illuminated entrance aperture, a special system of diaphragms is used. Two cameras

with a field of view of (15–84) $R_\odot$ and (66–318) $R_\odot$ are deployed on each STEREO spacecraft [29]. Coriolis, a US military satellite, detected CMEs and other heliosphere structures using SMEI (Solar Mass Ejection Imager), whose three wide-angle cameras, each having a field of view of $60^\circ \times 3^\circ$, could scan virtually the entire celestial sphere during a single 102-minute-long revolution of the satellite [30].

At the same time, detecting coronal radiation in the continuous spectrum from Earth's surface is also a task that is not doomed to failure. Based on the observation that corona radiation in the continuum is linearly polarized, and the polarization plane is always perpendicular to the radial direction from the disk center, several generations of instruments have been developed at Mauna-Loa observatory that enable separation of the coronal light from the scattered light. The accomplishment is facilitated by the high-altitude location of the observatory (more than 10,000 feet above sea level). COSMO K-Cor (COronal Solar Magnetism Observatory K-coronagraph), the last coronagraph in the series, yields an image of the corona beginning at a distance of $1.05\,R_\odot$ (up to $3\,R_\odot$) from the photosphere, a record unattainable by other space coronagraphs in operation [31]. COSMO K-Cor enables watching early stages of the onset of CMEs.

If multiple-antenna radio telescopes, often referred to as radioheliographs, are used to detect radio wave radiation from the corona, images of the corona can be produced with a spatial resolution high enough to explore motion in the corona in this spectral range [32]. Fluctuations of the parameters of radio wave emission from distant artificial and natural sources can be used to extract information about parameters of the plasma along the signal propagation path [33]. Using such radio screening sometimes enables the detection of CMEs and other perturbations of the solar wind that cannot be observed using other methods.

Space probes that measure solar wind parameters in situ at various points of space reliably detect the passage of magnetic clouds and CMEs of other types using characteristic changes in the solar wind density, velocity, and magnetic field. Some sensor of interplanetary plasma is installed on virtually every space station; there are also missions that are specially intended to monitor the solar wind. The Wind, ACE, and DSCOVR (Deep Space Climate Observatory) spacecraft, respectively launched in 1994, 1997, and 2015, are now located close to L_1, the Lagrangian point in the Sun–Earth system, at a distance of about 1.5 mln km from Earth. The measurements performed by these spacecraft not only provide data for studying solar wind properties but are also used for short-term alerts (~ 0.5 h) of geomagnetic perturbations.

3. Main properties of mass ejections in the solar atmosphere and interplanetary space

The initial phase of motion of matter away from the Sun is observed in lower layers of the solar atmosphere. Eruption of matter from the lower layers can be divided into two classes. The characteristic feature of the first class is that the erupted matter maintains its shape and increases in size, usually in the form of a loop that contains ejected matter (eruptive prominences) or that shapeless plasma lumps are abruptly ejected in all direction (flare sprays). The second class contains narrow collimated plasma streams of various scales (spicules, surges, and jets) [34–38].

Prominences are gas clouds located in the corona that have parameters typical of the chromosphere. The average dimensions of prominences are: length 50 Mm, height 10 Mm, and width several Mm [39]. The average density of particles in the prominence is $n \sim 10^{11}\,\mathrm{cm}^{-3}$ and the temperature $T \sim 7$ kK. The density in the prominence is thus two orders of magnitude higher than that in the ambient corona, while the temperature is two orders of magnitude lower. These factors maintain the balance of pressures on the boundary but fail to keep the prominence high in the corona due to the effect of the downward directed buoyant force. The dense matter can only be suspended by magnetic forces.

If these forces were absent, the matter would fall into the chromosphere under the effect of gravitation within a few minutes. To understand the magnetic nature of prominences, it is sufficient to look at their location on the Sun. A comparison with maps of the longitudinal (along the line of sight) photospheric magnetic field shows that prominences are always located on the boundaries of major areas with opposite polarity of the field (above the dividing line of radial field polarity) [40–45].

Activation of a prominence is sometimes initiated by observable external events, for example, a remote flare or rapid emergence of a new nearby magnetic flux, but most frequently the filament motion begins earlier than the manifestation of other nonstationary processes in the Sun's atmosphere. In most cases, there are no reliable pieces of evidence in favor of the existence of an external source. The very term used to describe this phenomenon observed on the disk, "sudden disappearance of the prominence," means that the onset of this process always occurs unexpectedly for observers. The prominences usually increase in size before the eruption, and they rise above the chromosphere. It has been noticed [46], however, that the prominences that attain a height of 50 Mm tend to an eruption that usually occurs within one or two subsequent days. The relation between the prominence height and length, which reflects the curvature of its axis, is of importance. If the ratio between the height of the middle part of the prominence to its length is less than 0.6, the prominence remains quiescent [47]. The existence of a limit height below which the equilibrium of prominences is stable is discussed below.

A prominence that is initially almost straight and horizontal bends in the vertical plane in the form of an arc whose ends remain fixed in the chromosphere (Fig. 1). Intermediate 'barbs' of the prominence detach one by one from the chromosphere, until only the two outermost barbs connecting the prominence body with the chromosphere are left. Velocity grows slowly at the onset of eruption, unlike the velocity of compact mass ejections (surges and sprays), whose acceleration is maximal at the initial stage [48]. The initial-stage velocity can be as low as several km s^{-1}. This feature is characteristic of both prominences in active regions and quiescent prominences; however, the length of the first phase of the former prominences is several minutes or about twenty minutes, while that of the latter can be as long as one to two hours. It is then followed by fairly rapid acceleration. The absolute value of the acceleration can be significantly larger than the free fall acceleration on the Sun's surface ($270\ \mathrm{m\ s}^{-2}$).

The eruptive prominence arc rapidly elongates upward, the elevation velocity being as large as several hundred km s^{-1}. Part of the matter flows along the arc bases downward to the

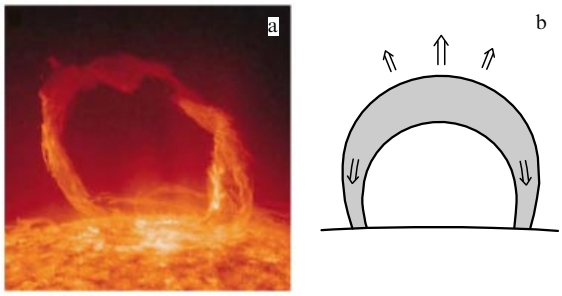

Figure 1. (a) Eruptive prominence (March 30, 2010) observed in the 304 Å channel of the AIA telescope aboard the SDO satellite. (b) Schematic rendering of matter motion in an eruptive prominence.

chromosphere (Fig. 1b), while another part gains a velocity sufficient to overcome the Sun's gravitational attraction (about 600 km s^{-1} near the surface) to become able to fly away into the interplanetary space in the ballistic mode. The downward motion of matter is evidenced not only by visible replacement of nodes and inhomogeneous areas in the prominence on the limb but also by measurements of the Doppler shift of spectral lines in the process of eruption on the disk. The central part of the eruptive prominence that corresponds to the arc top is visible in the bluer wing of the line, while the ends, which are close to the barbs, are observed in the redder wing. Owing to a decrease in density in the upper part of the loop as a result of its expansion and partial flowing down, the loop, observed in the Hα line looks as if it is disrupted; however, whenever images are available that are made using sufficiently wideband UV filters, the loop is seen to remain continuous despite its huge dimensions (Fig. 1a). Sometimes, an individual segment of a long prominence is destabilized, while other parts remain at their places. A layer detaches in some cases along the entire length of the filament that rises as a regular eruptive prominence, while the remaining part does not change its position [49, 50].

In moving away from the Sun, the eruptive prominence becomes part of a CME observable in white light (Figs 2 and 3). The mass ejection usually appears in the field of view of a coronagraph from behind the occluding disk as a bright protruding structure (see Fig. 2). As it develops, the following typical structure of the coronal ejection becomes visible: a loop-shaped frontal part that frames a rather extended dark cavity, in the center of which the brightest compact part of the mass ejection, a core, is located. A fibered twisted internal structure is sometimes visible in the core.

Several catalogs of CMEs based primarily on SOHO/LASCO observations are currently available wherein, however, the detected phenomena are identified in different ways. In the very first catalog, CDAW (Coordinated Data Analysis Workshop Data Center) (http://cdaw.gsfc.nasa.gov/CME_list) mass ejections were identified visually by an operator [51]. Several operators have been involved in this activity during SOHO/LASCO operations (more than 20 years), who subjectively select the events to be included in the catalog.

Other, more modern, catalogs operate based on automated computer methods for identification of CMEs. The Hough transformation was used in developing the CACTus catalog (Computer Aided CME Tracking catalog) (http://sidc.oma.be/cactus) [52, 53]. The system records many more events than are available in the CDAW catalog; however, the angular dimensions of more than half of these events are small

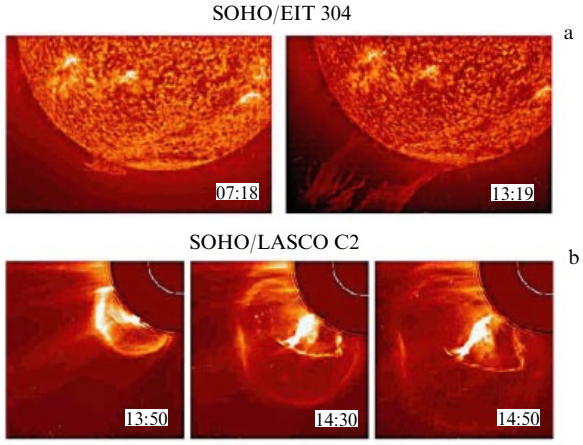

Figure 2. (a) Eruption of a quiescent polar-crown prominence (June 14, 1999) in the 304 Å channel of SOHO/EIT and (b) the subsequent CME seen in the SOHO/LASCO C2 coronagraph field of view. The single-color circle in the upper-right corners of Figs b corresponds to an external occluding disk of the coronagraph, while the white circle shows the solar disk size.

(less than 20°). In the ARTEMIS (Automatic Recognition of Transient Events and Marseille Inventory from Synoptic maps) catalog (http://lascor.oamp.fr/lasco/index.jsp), mass ejections are identified on pre-developed synoptic maps that correspond to a single Carrington rotation [54, 55]. The SEEDS (Solar Eruptive Event Detection System) catalog (http://spaceweather.gmu.edu/seeds/) uses a special algorithm transforming 2D difference images into one-dimensional arrays for automatic detection of mass ejections [56].

The angular (heliographic) dimensions of the CMEs are, on average, about 40° according to CDAW 'visual data' and do not exhibit a characteristic scale according to CACTus data distributed over a 20°–120° range as a power-law function with the exponent of about −1.7 [58]. There are, however, 'halo'-type mass ejections that populate the entire

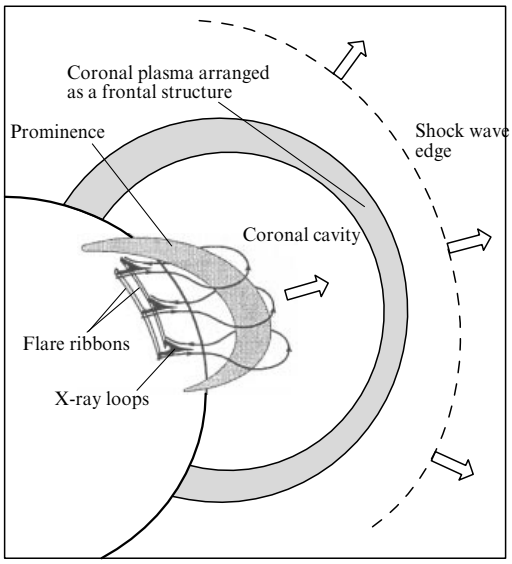

Figure 3. Schematic rendering of the structure of a CME that consists of a prominence forming a core, a dark cavity around it, an external frontal loop consisting of collected compressed coronal plasma, and an excited shock wave [59].

360-degree area around the occluding disk. These are the mass ejections that originate close to the solar disk center and move towards Earth or in the opposite direction.

The velocity with which the frontal edge of the mass ejection moves in the coronagraph field of sight is essentially the minimal estimate of its velocity, because it does not take motion along the line of sight into account. Mass ejections are observed whose velocities are distributed in a wide range from 20 km s^{-1} to more than 2,500 km s^{-1}, with the mean $\sim$ 500 km s^{-1} [57]. Slower mass ejections usually move with an acceleration of the order of 10 m s^{-2}, while in some cases the acceleration is as large as 1,500 m s^{-2}, a value that is five times higher than the free-fall acceleration on the Sun. Fast mass ejections usually lose velocity with a deceleration of 5–20 m s^{-2} [60]. The mass of the matter dragged by a CME depends on its size and density and ranges within 10^{14}–10^{16} g, with the mean about 2×10^{15} g [61]. The mean kinetic energy of a mass ejection is consequently $\sim 10^{23}$ J.

The number of CMEs observed in the minimum of the solar activity cycle is on average one per day, but if the number of spots increases, the frequency of mass ejections virtually synchronously increases to approximately 4–8 events per day [24]. CACTus data for the 23rd cycle show that the average number of mass ejections is delayed with respect to changes in the Wolf number by 6–12 months [53]. In solar activity minima, the mass ejections are primarily observed close to the equatorial plane, where coronal streamers are also located. In the cycle maximum, both mass ejections and streamers are observed at all heliographic latitudes.

If projected onto the plane of the sky, many CMEs have the shape of a cone whose vertex is located in the Sun's center, and a hemisphere supported by the cone base. The shape of mass ejections resembles an ice-cream cone; it is for this reason that a model describing geometric and kinematic characteristics of mass ejections was named the 'ice-cream cone model' [62]. This shape persists during the entire time that the mass ejection passes across the coronagraph field of view, without changing its angular opening. The actual direction of the cone axis is determined by fitting model parameters to measurements made at various points of the mass ejection projection. The conic model enables forecasting the arrival of CMEs on Earth to be significantly improved [63]. It is not infrequent that the upper part of the mass ejection is flattened and thickened. A mass ejection with this shape is seen as a mushroom-shaped cloud (a cap on two legs) in the Sun's corona [64].

The arrival of a CME to the point where a space probe detects solar wind parameters is characterized by the following signatures that can be exhibited in various combinations depending on the specific event [65]: 1) an increased magnetic field; 2) gradual change in the field direction; 3) relatively low proton temperature; 4) small value of the plasma β parameter; 5) bidirectional flows of electrons (in two opposite directions along the local magnetic field); 6) bidirectional flows of low-energy protons; 7) high degree of ionization of elements and specific features of their composition; 8) low degree of ionization; 9) single-ionized helium atoms; 10) bidirectional flows of fast particles ($\sim$ 1 MeV); 11) bidirectional heat flows; and 12) coincidence with a terrestrial Forbush decrease in the cosmic ray flow. Magnetic clouds are usually identified on the basis of signatures 1–4, also assuming that the presence of signature 2 actually requires not only the field direction to change but also its vector to rotate smoothly.

An analysis of data spanning almost two solar cycles has shown that the annual average number of both ICMEs and the number of mass ejections observed close to the Sun varies synchronously with the Wolf numbers (from $\sim$ 5 to $\sim$ 40) [18, 66]. However, the number of detected magnetic clouds depends very weakly on the cycle phase, because their fraction in the total number of ICMEs significantly increases in the years of minimum activity. A structure typical of the magnetic clouds is arguably present in most of the ICMEs detected at the maximum of activity; however, it can sometimes be faintly exhibited as a result of the tangential passage of the observation point, because sources on the Sun can be located at high altitudes far away from the ecliptic plane in which the detecting probes are located. The average of the absolute value of the magnetic field in ICMEs is 10 nT, the average velocity is 450 km s^{-1} m, and the average proton temperature is 50 kK, the median values being somewhat smaller [18].

To reconstruct the spatial structure of ICMEs on the basis of time profiles of the quantities measured at the same point, some model approaches are used (Fig. 4). The simplest magnetic-flux-rope model has been developed in the approximation of a force-free field [68]:

$$\nabla \times \mathbf{B} = \alpha \mathbf{B}\,, \tag{1}$$

$$B_z = B_0 J_0(\alpha\rho)\,, \tag{2}$$

$$B_\rho = 0\,, \tag{3}$$

$$B_\varphi = B_0 J_1(\alpha\rho)\,, \tag{4}$$

where z, ρ, and φ are cylindrical coordinates, B_0 is the magnetic field amplitude, J_0 and J_1 are the cylindrical Bessel functions of the zeroth and first order, and α = const.

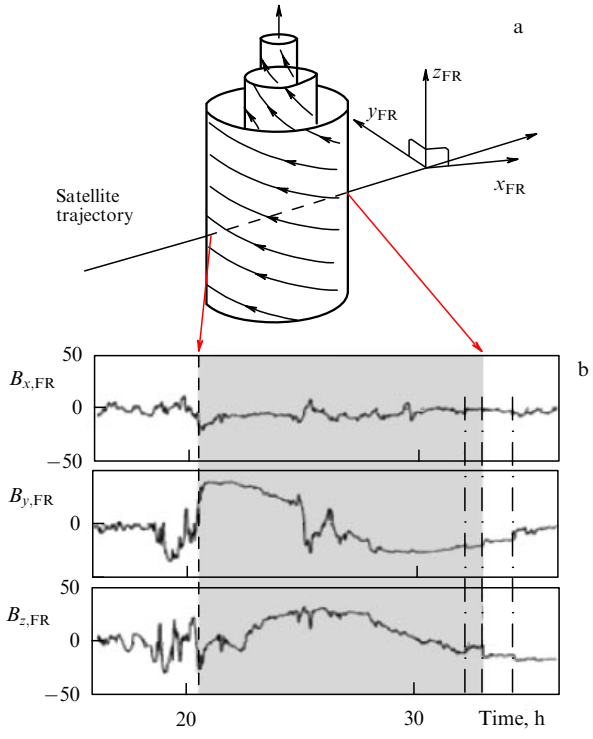

Figure 4. Hypothesized structure of the magnetic flux rope of a CME and changes in the components of the magnetic field detected by a satellite during passage of the mass ejection [67].

The direction of the magnetic field component that does not change sign and attains its maximum in the central part of the cloud sets the orientation of the magnetic-flux-rope axis. If a probe passes approximately through the cloud center, as can be determined based on the symmetry of profiles, the field component that corresponds to the radial field of the flux rope is negligibly small along the trajectory, while the third component, which corresponds to the azimuthal field of the flux rope, changes sign in the cloud center. This simple model with axial and translation symmetry describes the local structure of the magnetic cloud. Models where the cross section of the flux rope is not circular [69] or the assumption that the field is force-free is abandoned [70, 71] can be regarded as a development of this model.

To reconstruct the magnetic cloud structure, the Grad–Shafranov equation with translation symmetry ($\partial/\partial z = 0$) is widely used, which describes magnetohydrostatic equilibrium of plasma,

$$\frac{\partial^2 A}{\partial x^2} + \frac{\partial^2 A}{\partial y^2} = -\mu_0 \frac{\mathrm{d}}{\mathrm{d}A}\left(p + \frac{B_z^2}{2\mu_0}\right), \tag{5}$$

where $\mathbf{A} = A(x, y)\mathbf{e}_z$ is the vector potential, p is the plasma pressure, and μ_0 is the magnetic permeability [72].

The magnetic field is considered in the models described above as a static magnetic flux rope. Dynamic models take into account that the cloud expands in the process of observation. Some models only assume that the circular cross section radius increases [73], while in other models the flux rope expands in all three dimensions [74]. The expansion along the radius alone violates the force-free configuration of the flux rope and induces a significant imbalance of forces in the process of cloud evolution, while observations show that β is small, thus requiring magnetic strains to be balanced. Isotropic expansion does not violate the balance of forces, but the requirement of isotropic expansion does not compare well with the anisotropy of magnetic forces in the flux rope. The expansion of the magnetic cloud on its way from the Sun to the point of measurement is due to the ambient environment pressure decreasing as $\approx D^{-2.9\pm0.3}$, where D is the distance from the Sun. The magnetic flux rope radius R then increases with the distance as $D^{0.9\pm0.3}$ [75]. The magnetic flux and helicity in the magnetic cloud are approximately preserved, while the magnetic energy decreases in approximately inverse proportion to the distance [76].

As long as the mass ejection remains in the field of view of coronagraphs, the bases of its expanding loop usually remain fixed in the lower layers of the Sun's atmosphere. Therefore, cylindrical models definitely do not correspond to reality. A hypothetical view of a mass ejection in the heliosphere is shown in Fig. 5. An important argument in favor of magnetic coupling being maintained between the magnetic cloud and the Sun is that bidirectional flows of fast electrons are observed within a cloud whose mean free path compares well with the magnetic flux rope structure. The axial curvature of the magnetic flux rope is taken into account in toroidal models. The toroid in simpler models is concentric with the Sun and in no way is related to its surface [77, 78].

Because parameters of interplanetary ejections vary in a broad range, it cannot be ruled out that some magnetic clouds fully detach from the Sun and move like isolated structures. A toroid is a good approximation for clouds of that kind. Cloud dimensions may be not large, while the density and magnetic field can exceed expected values. A configuration referred to as a spheromak can be used as a model of such compact magnetic clouds. A solution of Eqn (1) for a force-free field in the lowest order (beyond the monopole) in spherical coordinates r, θ and φ has the form [79]

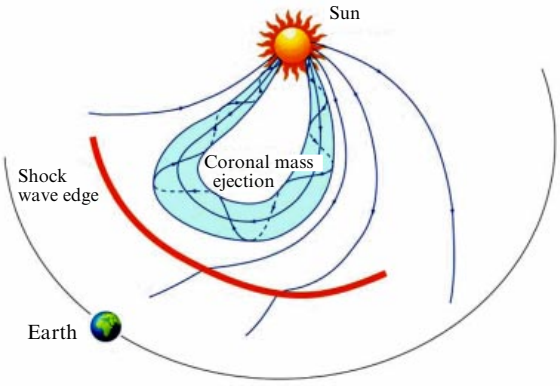

Figure 5. Interplanetary coronal mass ejection in the heliosphere.

$$B_r = \frac{2B_0}{\alpha r} j_1(\alpha r)\cos\theta, \tag{6}$$

$$B_\theta = -\frac{B_0}{\alpha r}\left(\sin\alpha r - j_1(\alpha r)\right)\sin\theta, \tag{7}$$

$$B_\varphi = \pm B_0 j_1(\alpha r)\sin\theta, \tag{8}$$

where j_1 is a spherical Bessel function of the first order. The magnetic field described by Eqns (6)–(8) is often referred to as a 'classical spheromak'. It is this spheromak-type configuration that has proved to be the most suitable for interpreting the causes and circumstances of the strongest geomagnetic storm observed in the 23rd solar cycle [80].

In simulating the evolution of CMEs in the heliosphere in a magnetohydrodynamic (MHD) approximation, the magnetic flux rope is embedded into the solar wind as the initial condition [81, 82]. Computations usually show that the magnetic flux rope moves faster than the ambient solar wind. The cross section of a flux rope that was initially circular increases owing to expansion and acquires an oval shape compressed in the direction of motion due to the dynamic pressure of the solar wind flow that it catches up with. Some calculations [83] predict that owing to interaction between the initial spheromak and the radially expanding stationary solar wind, the spheromak transforms into a toroid.

Presenting the CME as a magnetic flux rope describes its local internal structure and evolution at certain stages of its development. To track how the mass ejection evolves over longer distances, simple phenomenological models, similar to the 'ice-cream cone model', should be used.

4. Relation of coronal mass ejections to eruptive prominences and other manifestations of solar activity

Transformation of an eruptive prominence into CMEs in a series of events like that shown in Fig. 2 raises no doubts. But because eruptive prominences and coronal mass ejections are observed in various parts of the spectra using various

instruments whose fields of view do not overlap, their relation has not always been obvious and required special examination. Statistical studies showed from the very beginning that eruptive prominences are the manifestation of activity in the lower layers of the Sun's atmosphere, with which ejections correlate most strongly [84–87]. The height at which the eruptive prominence is observed is an important factor: the larger height it attains, the higher the probability that it would be followed by a CME.

For example, it was shown in [85] that all the prominences that reached a height of $1.2\,R_\odot$ and only 60% of those that reached a height of $1.1\,R_\odot$ were related to CMEs. A terminological issue emerges here: can the term 'eruptive' be used for prominences and filaments that initially rise fairly rapidly maintaining their overall shape and then decelerate and halt, thus exhibiting finite motion? It was proposed to call such prominences simply 'active' [88] and the eruptions 'failed' [89–93].

In 1996–1998, 46% of such active prominences and 94% of 'true' eruptive prominences that were able to overcome the Sun's gravitational attraction were related to CMEs [88]. Mass ejections related to eruptive prominences typically have a bright core, unlike the mass ejections related to the activation of prominences. Among 50 eruptive prominences observed in 1999–2000 in the microwave range by the Nobeyama observatory's NoRH heliograph (Nobeyama RadioHeliograph), 92% were accompanied by CMEs [94]. A larger array of observational data collected using the same instrument in 1996–2001 (186 eruptions) shows that the eruptive prominence was followed in 72% of cases by CMEs, while the fraction of such events for prominences that move predominantly in the radial direction increased to 83%.

Statistical studies that are based on data arrays selected using certain criteria heavily depend on the choice of those criteria that are not always objective and may vary depending on the specific research team. This also refers to considering or disregarding very narrow or low-contrast mass ejections or categorizing as eruptive processes events of 'thermal' disappearance of filaments (i.e., those that disappear from images of chromosphere spectral lines due to temporary heating) or failed eruptions.

For example, a very low correlation, 10%–30%, between the disappearance of filaments in the Hα line and CMEs [95] was likely due to taking the events of thermal disappearance into account. If such disappearance events are intentionally excluded, the correlation factor increases to 52% [96], while correlation within a similar period with eruptive prominences observed in the radio wave range is 65% [97].

The distribution of eruptive prominences over the heliolatitude differs from that of mass ejections. The former events are observed most frequently at latitudes of $\pm 30^\circ$, while the latter concentrate near the equator and rather uniformly populate all latitudes when the solar cycle comes closer to the maximum [97, 98]. The difference is most probably related to modifications in the structure of the coronal magnetic field as height changes. Because both the prominences and CMEs cluster about polarity inversion lines (PILs), their lateral distributions reflect the position of those lines in fields of different scales. At smaller heights, where prominences are located before the eruption, a significant role is played by fields of a smaller scale, which are represented by higher harmonics in the expansion of the global magnetic field in spherical functions. The octupole dominates near the photosphere even in the minimum of activity; but because it decreases as the distance grows faster than the dipole component, at distances larger than the Sun's radius, where mass ejections are observed, it is replaced with the dipole directed approximately along the Sun's rotation axis. Owing to this, the eruptive prominences that originate from higher latitudes keep close to the PILs on the corresponding height (or a neutral surface drawn on these lines) and do not rise vertically but deviate on average to the equator. This nonradial motion of the eruptive prominences is observed in many events [99–104].

Flares were initially considered a generator of CMEs that were assumed to be just a hydrodynamic response of the solar atmosphere to an abrupt release of energy in the flare [105, 106]. However, this concept was soon abandoned for a number of reasons, including energy considerations and the long time during which the mass ejections are accelerated [59]. Most optical flares occur independently from mass ejections, while those that coincide with mass ejections are their consequence rather than the cause [19]. However, the largest and fastest mass ejections are related to large two-ribbon flares. Optical flares exhibit a rather close relation to frontal halo-type CMEs that move towards Earth [107, 108].

X-ray radiation is commonly used as an indicator of flares in correlation-analysis studies because extraterrestrial observations are more regular and uniform. The flares can be well classified using the maximum X-ray radiation flux (introducing classes from A to X, whose respective intensity is less than 10^{-7} W m^{-2} and more than 10^{-4} W m^{-2}). An analysis of data obtained using the LASCO coronagraph showed that $\sim 70\%$ of class-C flares, $\sim 40\%$ of class-M flares, and $\sim 10\%$ of class-X flares are not related to CMEs, and the probability of detecting a mass ejection does not depend on the location of the flare on the Sun's disk [109–111]. There are thresholds for the maximum intensity (6×10^{-5} W m^{-2}), total flux (7×10^{-2} J m^{-2}), and duration (4h), an excess of which enables predicting with a 95% probability that a CME will be observed along with the flare. If these quantities are lower than the specified thresholds, no significant dependence of the ejection probability on the maximum intensity or duration of the flare is observed. If the total flux increases, the fraction of mass ejections that accompany the flare also increases.

Regarding characteristics of the mass ejections themselves, a stronger relation with the flares is observed for fast mass ejections that exhibit a constant velocity or a small deceleration [112–115]. There are also observational data [116–118] that show that the fast-acceleration stage of mass ejection coincides in most cases with an increase in the flare radiation intensity; however, the acceleration begins, as a rule, prior to the emergence of a soft-X-ray radiation surge and ends when its maximum is attained [119].

The total number of mass ejections whose kinetic energy exceeds a specific energy as a function of that energy (the integral energy spectrum) is described by a power-law function with the exponent close to -1 [120]. The same exponent for flares is about -2 [121, 122]. A difference this large between the two values probably implies that the energy conversion mechanisms operating in these two phenomena are very different. In the opinion of the overwhelming majority of researchers, there is neither mutual correspondence nor a direct cause–effect relation between the flares and mass ejections, and both phenomena evolve as a result of instability of magnetic structures in the Sun's atmosphere, which causes both thermal effects (flares) and motion of plasma (eruptions and mass ejections). Depending on specific conditions, both

effects can manifest themselves in a single event to various degrees or not be manifested at all [24, 123, 124].

Long-lived arcades of post-flare loops emerge at the late stage of major flares that can be observed in soft X-ray and extreme UV ranges [125, 126]. The bases of the loops coincide with flare ribbons. As the ribbons move away from each other, the height of the loops increases. The arcades are related more closely to coronal ejections; therefore, their second name is post-eruptive arcades. Mass ejections with a suitable location and eruption onset time have been found for 92% of arcades among the 236 arcades explored in [127].

Mass ejections are related even more closely and on more justified grounds to coronal dimmings, areas of decreased radiation observed in the soft X-ray [128, 129] and extreme UV [130, 131] ranges and even in the Hα line [132], which emerge after eruptive events. Dimmings have been observed in about 30% of cases of halo-type ejections [133]. Given that half of the events originated on the other side of the solar hemisphere, the correlation doubles to attain 60%.

Development of dimming attains a maximum when the mass ejection has already passed a distance equal to several solar radii [134–136]. Dimming is usually seen on the disk in UV coronal lines as two similar irregularly shaped dark spots on both sides of the vanished filament ends. Radiation flux on the 195 Å line in dimming is $\sim 25\%$ of the flux that was emitted from that region prior to an eruption [137]. Dimming is located at a height ranging from 0.1 $R_\odot$ to 1.5 $R_\odot$ above the surface [138] and frequently occurs after the passage of the spherical front of a coronal wave (EIT wave, a wavelike phenomenon named after the Extreme Ultraviolet Imaging Telescope on board SOHO, with which it was discovered); however, it may exist for a long time, hours or days. The corona mass deficit associated with dimming is of approximately the same order as the mass contained in the mass ejection [139].

Dark areas in X-ray and UV images may be due to both a reduction in the density of radiating plasma and changes in temperature. It is virtually impossible to separate these effects using filtered images alone; however, spectroscopic data reveal the presence of Doppler-shifted lines that evidence the outflow of matter from the dimming area with velocities ~ 30 km s^{-1} [138]. A formal resemblance to coronal holes prompts a conclusion that dimmings are short-lived (transient) coronal holes, i.e., areas of open field lines [140]. The dimmings are probably areas where the erupted magnetic structure remains linked to the surface; indeed, the magnetic field in these areas extends into the interplanetary space [133]. The magnetic flux of the photosphere field integrated over the dimming area correlates well with the ejection velocity in the coronagraph field of view [142, 143] and can be used as an indicator of the geoeffectiveness of a mass ejection [143, 144].

The set of other sporadic phenomena that accompany CMEs includes coronal waves [130, 145, 146], type-II and IV radio bursts [85, 147, 148], coronal and interplanetary shock waves [149–153], and energetic particles [154–156]. However, although the number of phenomena that usually accompany the emergence of CMEs is large, mass ejections are observed with which no manifestation of activity in the lower layers of the Sun's atmosphere can be associated. Prior to the launch of the STEREO spacecraft, all halo-type ejections that had no visible manifestations on the Sun's disk were categorized as ejections that originate from the other side of the solar hemisphere and move in the direction away from Earth. However, some of those mass ejections were accompanied, after a certain time elapsed, by geomagnetic storms. Such 'problematic' storms without visible manifestations of near-surface solar activity have been known since before the era of regular observations of the solar corona by spacecraft [157]. STEREO observations made from various viewpoints have shown that mass ejections can originate on the Sun's visible part without other manifestations of the activity [58, 158–160]. Such mass ejections, which are referred to as 'stealth' events, usually feature low contrast and move with a very small velocity (< 300 km s^{-1}). Nevertheless, much attention is paid to exploring stealth mass ejections, because they can cause geomagnetic storms that are difficult to forecast.

5. Magnetic configurations as mass ejection movers

Most modern models hypothesize that the cause of the occurrence of CMEs is violation of the equilibrium and stability of coronal magnetic fields. Magnetic fields on the Sun are primarily generated under the photosphere surface in the convective zone. A question arises: how rapidly can the magnetic flux that carries the corresponding energy penetrate into the corona and initiate an eruptive process? In the opinion of some authors, such pumping with energy can occur directly in the process of eruption. For example, as a result of pulse injection of a poloidal magnetic flux, the stability of a twisted coronal magnetic tube is violated, and it elevates with acceleration [26, 161], or a magnetic flux rope flies out with a supersonic speed from the convective zone [151].

However, observations of photospheric magnetic fields do not confirm these fast changes in the fields that are required by the mechanisms of direct energy transfer from the convective zone to the areas where the mass ejections are formed. It is therefore most probable that the energy needed for a mass ejection to occur is slowly accumulated in the corona owing to gradual emergence of new magnetic fluxes from beneath the photosphere and photosphere motions. The nonpotential part of the coronal magnetic field, i.e., the electric currents flowing in the corona, serves as a reservoir for that energy. This is evidenced by the magnetic energy density in the corona being several orders of magnitude larger than that of other kinds of energy [59].

Modern models are based on modifications of the two main initial magnetic configurations where instabilities develop under the effect of various external factors resulting in an eruption: an arcade of loops with the bases displaced in opposite directions along the central axis and a magnetic flux rope. The shift of the magnetic loop bases in opposite directions along the PILs of the photospheric longitudinal magnetic field, also referred to as 'shear', i.e., nonperpendicularity of the field lines and PILs, is often regarded as evidence of the presence of an electric current, although actually this is not true. An angle between a field line and a PIL other than the direct angle can also occur in a potential (current-free) field. Strict perpendicularity is only observed in symmetric fields. Nevertheless, the threads that are observed in the fine structure of filaments (regarded as one of the main pre-eruptive structures) and which are directed along a PIL or make an acute angle with it, prompted the development of models of prominences and mass ejections based on shear motions of field-line bases in a narrow stripe near a PIL.

Initially convex flux tubes become depressed in the upper part as a result of such motions, and the horizontal field

component in the depressed part can be directed not only along the PIL but also at some angle from the negative photosphere polarity to the positive one. The depressions in force tubes are suitable for accumulating dense plasma; calculations done in numerical MHD models show that an excess of magnetic energy over the energy of the initial potential field appears in the coronal field [162, 163]. Coronal electric current creates a magnetic pressure that tends to push out the current and extend the arcade. On the other hand, the external loops of the arcade that are not displaced create a tension that confines the internal system of currents. This mutual counteraction enables accumulation of free magnetic energy in an amount sufficient to accelerate a mass ejection; however, for the ejection to occur, it is necessary to overcome confining forces during a short time and enable matter to accelerate.

In ideal MHD, a simple arcade preserves its stability under any shear [164] to transform in the limit into a system of open field lines with an infinitely thin layer of currents that delimits opposite polarities. Moreover, the energy of this fully open field is maximal among the energies of all possible configurations of a force-free field whose field-line bases are fixed in the photosphere [165–167]. As a result, it is energetically disadvantageous for the arcade to go out into interplanetary space in the form of a CME.

A way to overcome this constraint was proposed in the breakout model in a quadrupole configuration [167–170]. The central arcade subject to shear deformation is sandwiched between two side arcades that have common field lines on the periphery. When the central arcade rises, part of its magnetic flux reconnects with these force lines, thus increasing the magnetic flux of the side arcades (Fig. 6). As a result, the containing field weakens and may be completely removed, while the overall flux remains predominantly closed, thus eliminating the constraint set by the maximum energy of the open field [165–167]. A similar analytic model of field breakout with the formation of a CME had been proposed earlier in a geometry that features translation symmetry and a rising magnetic flux [171]. Numerical calculations [172, 173] later showed that the emerging magnetic flux can break through the corona field in an imitation of a mass ejection.

The sheared arcade at later stages of its evolution insignificantly differs from a magnetic flux rope whose magnetic vector rotates by an angle slightly smaller than full revolution, and it transforms into a full-fledged flux rope as a result of reconnection [169, 174, 175]. It is already at the main stage of its acceleration that the CME configuration is most probably a magnetic flux rope. At the same time, much evidence has been collected recently that flux ropes are present in the solar atmosphere long before eruptions [176, 177]. A magnetic flux rope can form in a corona as a result of various motions of field line bases in the photosphere followed by reconnection of deformed lines. In addition to shear motions, the formation of flux ropes is facilitated by flows converging to PILs [178, 179], rotations [180, 181], and mutual cancelation of magnetic fluxes of opposite polarity [182, 183].

Another way for magnetic flux ropes to emerge in the corona is the rise of a well-developed flux rope from the convective zone (Fig. 7). A twisted magnetic tube rises to the photosphere owing to magnetic buoyance [184]. It significantly expands there and starts penetrating into the corona. If the tube were absolutely straight, the dense matter within it would remain in its lower part due to being embedded, and the tube would only be able to rise into the corona as high as half of the diameter [185]. But because the axis is bent (Fig. 7a), matter can flow down to the immersed parts of the tube, thus allowing some segment to fully rise into the corona [186, 187]. Specific features can sometimes be revealed in detailed observations of photospheric magnetic fields that are interpreted as changes related to the passage of magnetic flux ropes from the photosphere to the corona [188–190].

An question of importance for simulating eruptive phenomena is: what is the total current in a magnetic flux

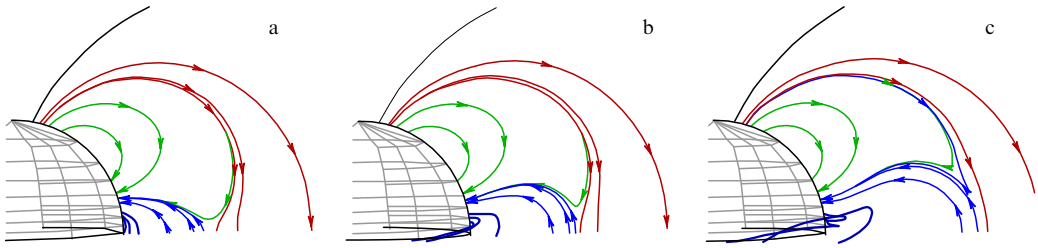

Figure 6. Evolution of field lines of the coronal magnetic field in the 'breakout' field model [168].

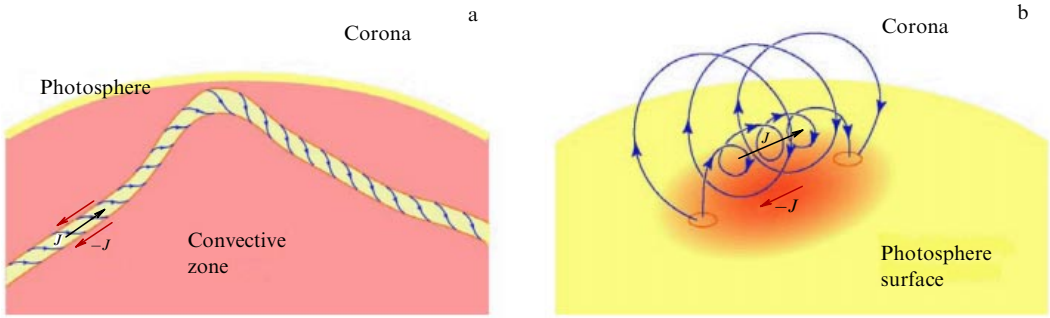

Figure 7. Upward motion of a magnetic flux rope from the convective zone to the corona.

rope? The twisted magnetic tube is surrounded in the convective zone by dense plasma that does not allow its magnetic field to propagate far away. If the total current flowing through the tube cross section is J, the reverse current $-J$ emerges on its boundary that fully compensates the forward current in the tube (Fig. 7a). Such a flux rope is sometimes referred to as shielded or neutralized. If a tube like this reaches the rarified corona, it can expand after having released most of its matter. The boundary at which the shielding current can be confined for a typical coronal flux rope with a forward current of 10^{11}A [191–194] moves away from the flux rope axis by half the solar radius [195]. However, the return current can definitely persist on the photosphere surface (Fig. 7b). Results of both an analytic model [196] and numerical MHD simulation [197] show that the return current remains in the photosphere as the twisted tube moves upward. The presence of an uncompensated electric current in coronal flux ropes is actually indicated by the location of the filaments associated with them along the PILs of the photospheric magnetic field. This observation implies that the integral current of flux ropes interacts with the external magnetic field.

The magnetic flux rope in the corona is subject to the force [198]

$$\mathbf{F} = \frac{1}{c}\int_V (\mathbf{j}\times\mathbf{B}_\mathrm{f})\,\mathrm{d}v + \frac{1}{c}\int_V (\mathbf{j}\times\mathbf{B}_\mathrm{e})\,\mathrm{d}v - \oint_S p\mathbf{n}\,\mathrm{d}s + M\mathbf{g}\,, \quad (9)$$

where V is the volume occupied by the flux rope, S is the outer surface of the flux rope, $\mathbf{n}$ is the normal to the surface, $\mathbf{j}$ is the density of the electric current in the flux rope, $\mathbf{B}_\mathrm{f}$ and $\mathbf{B}_\mathrm{e}$ are the magnetic fields generated by the currents inside the flux rope and the external currents, p is the gas pressure, M is the mass of plasma contained in the flux rope, and $\mathbf{g}$ is the free fall acceleration on the Sun. The force $\mathbf{F}$ must be zero in the initial equilibrium state. If the transverse dimension of the flux rope is smaller than other characteristic dimensions, and the external field and external pressure can be considered constant within the cross section, the equilibrium condition decomposes into two separate conditions. The first determines the equilibrium of the flux rope as a whole:

$$\frac{1}{c}\,\mathbf{J}\times\mathbf{B}_\mathrm{e} + m\mathbf{g} = 0\,, \quad (10)$$

where

$$\mathbf{J} = \int_A \mathbf{j}\,\mathrm{d}s \quad (11)$$

is the total electric current flowing through the cross section A of the flux rope and m is the mass per unit length of the flux rope. The second condition describes the balance of forces inside the flux rope:

$$\frac{1}{c}\,\mathbf{j}\times\mathbf{B}_\mathrm{f} = \nabla p\,. \quad (12)$$

6. Instabilities of equilibrium that lead to eruption of magnetic flux ropes

Free magnetic energy accumulates in the corona as a result of slow changes in the photosphere. The characteristic time during which this energy is released in eruptive processes is two to three orders of magnitude smaller than that of photospheric motions. Mechanisms for the generation of coronal mass ejections must be based on the development of some unstable structures of magnetic configurations in the corona, the impacts of which are catastrophic.

The long twisted flux tube is subject to instability with respect to kink twisting. As a result of the development of this instability, some parts of the tube can rise, and loops and 'kinks' can emerge, thus initiating eruption. The kink instability develops in a force tube with the surface current if the twist angle φ that the field line accumulates on the tube length L exceeds a threshold value (the Kruskal–Shafranov condition [199]),

$$\varphi = \frac{L}{R}\,\frac{B_\varphi}{B_z} > 2\pi\,, \quad (13)$$

where B_φ and B_z are the azimuthal and longitudinal components of the field and R is the tube radius. If the current is distributed over the tube cross section, the instability threshold changes. For example, instability occurs for a force-free field with the twist angle constant over the cross section [200] if $\varphi > 2.5\pi$ [201]. A stabilizing effect is provided by field lines at the ends of the loop-like tube being 'frozen' into the dense photosphere plasma, as a result of which they cannot move. The kink instability threshold in numerical MHD models of the evolution of twisted coronal magnetic loops whose ends are fixed in the photosphere can be as large as 3π to 4π [202–206].

Helical threads are not infrequently observed in quiescent prominences and ambient coronal structures, but more frequently in the process of activation and eruption of prominences [176, 192, 207–209]. Tracking an individual flux tube from the beginning of the flux rope to its end can be difficult due to the inhomogeneity of the plasma that fills the tube and the mutual overlap of the threads that constitute a kind of a multiple-thread screw. Therefore, the accuracy of estimated twist angles or the number of total revolutions of field lines is not high. Noticed in events related to the activation of filaments, eruptions, and flares are twists consisting of 2–3 full revolutions [210–212] or even 3–4 revolutions [213, 214], values that significantly exceed the kink instability threshold. Based on this, the authors of the quoted studies consider the kink instability to be an initiator of observed active phenomena. On the other hand, calculations of the structure of the coronal nonlinear force-free magnetic field based on the field vector distribution in pre-eruptive areas in the photosphere yield moderate values of field-line twists in flux ropes, not exceeding one and a half revolutions [215–220].

The twist of field lines around the flux rope axis transforms at the nonlinear stage of the development of kink instability into a writhe of the flux rope axis itself [221]. If a rubber band is twisted, 'kinks' are created in a similar way. The vertical equilibrium of the current is influenced by the horizontal external field; but because the horizontal equilibrium is attained on a 'neutral line', where the vertical field is zero, the horizontal component constitutes the entire field. Above the axis, this field is approximately aligned with the flux rope's own azimuthal field, and below the axis its direction is opposite to that of the azimuthal field of the flux rope. If the coronal field changes relatively slowly as height increases, then, as numerical MHD simulations show, the loop decelerates and halts after an initial fast rise, thus exhibiting an example of a 'failed eruption' [90]. If the coronal field decays rapidly, eruption continues to evolve into a CME [90, 222].

If the vertical gradient of the external field is large, the equilibrium of the flux rope can become unstable if the

current is smaller than that needed for the kink instability to develop. The possibility of such instability has been demonstrated using simple models wherein the magnetic flux rope is represented by a linear electric current [223–226]. The equilibrium of the filament current is determined by the balance of the magnetic pressure created by the field among the filament and the photosphere, the magnetic strain of the confining field, and the filament weight. The main mass in the coronal flux rope is concentrated in the prominence it contains. If standard estimates are used for coronal currents and prominence masses, the gravitational force is 1–2 orders of magnitude smaller than the magnetic pressure forces and the strain that determines the equilibrium of the flux rope at the height h. The magnetic pressure creates a force equivalent to the effect of a reverse current at the depth $-h$ below the photosphere surface (mirror image of the coronal current). The field it generates decays as h^{-1} with height. If the confining field decays more slowly, the equilibrium of the flux rope is stable, and if faster, it is unstable. The confining field can be characterized using a decay index equal to the exponent of the locally approximating power-law function $B \sim h^{-n}$, defined as [227, 228]

$$n = -\frac{\partial \ln B}{\partial \ln h} . \tag{14}$$

If as a result of evolution the flux rope attains the critical point where $n = 1$, it loses stability and begins rising while rapidly accelerating.

Because photospheric fields occupy large areas, the field decays at small heights slowly ($n \ll 1$), and the equilibrium of coronal magnetic flux ropes is stable. As height increases, the field decays more rapidly (the potential field decays at long distances from sources as a dipole field, for which $n = 3$), and there is always a critical height h_c above which the equilibrium becomes unstable. If the electric current in the flux rope increases in the process of evolution, the height of its equilibrium position increases and when the critical height is attained for the current $J = J_c$, the flux rope becomes unstable and can no longer exist at larger heights, $h > h_c$. Eruption of the flux rope occurs. This scenario was named the catastrophic equilibrium loss [77, 198, 229–234].

If the flux rope axis is bent, an additional force emerges that acts on each length element from the side of other segments. The nature of this force has been analyzed in detail for toroidal systems of laboratory plasma confinement [235]. A thin toroidal flux rope is in stable equilibrium in an external magnetic field perpendicular to the torus plane if the field has an appropriate value and decays in the radial direction no faster than $R^{-1.5}$ [236–238]. If the field decays faster, the equilibrium is not stable, and if the decay exponent varies with changes in radius, the same catastrophic loss of equilibrium can occur as in the case of the straight current. Due to the specific geometry, this instability was named 'torus instability'. The concept of the catastrophic loss of equilibrium assumes that system parameters evolve in a way that leads to a catastrophe. An analysis of instability requires the behavior of small perturbations to be examined at fixed parameters. If applied to the onset of the eruptive process in the corona, both approaches are equivalent because they are based on the balance of the same forces and initiate eruption under the same conditions [239, 240].

The accurate value of the critical decay exponent n_c at which instability of the vertical equilibrium of the magnetic flux rope evolves depends on the parameters of the model and the assumptions made. The value of n_c is also affected by the geometry of the flux rope axis, anchoring the flux rope ends in the photosphere, the ratio of the loop length and its transverse size, etc. The critical exponent n_c for a flux rope that has a significant cross section and with either a straight or bent axis falls in the range 1.1–1.3 if the cross section increases in the process of eruption and 1.2–1.5 if it remains unchanged [239].

Some models are based on an assumption that under the conditions of high coronal plasma conductivity, field lines cannot change their connectivity, i.e., 'reconnect'. In that case, some deformations of the field due to changes in photospheric boundary conditions are supposed to result in the creation of current sheets in the photosphere. These sheets accumulate the significant amount of free energy that cannot dissipate due to high conductivity. If at some moment the conductivity rapidly decreases (for example, due to development of turbulence), the field lines separated by current sheets start rapidly reconnecting, and the energy of the current sheets starts transforming into the energy of another kind, thermal or kinetic. The strain of confining field lines can weaken as a result of reconnecting, and the structure it confines can expand and move upward. This mechanism of initiation of eruptions is referred to in some models as 'tether cutting' [241]. Reconnection undoubtedly plays an important role in the evolution of the coronal field and changes in its structure and topology. It is not clear, however, in what way the connectivity rapidly changes, causing fast nonstationary processes.

We note that the initial phase of the magnetic flux rope eruption, catastrophic loss of equilibrium, is well described within an ideal MHD. However, the increasing strain of upward-moving coronal field lines, which cannot disrupt and reconnect under ideal conductivity, prevents the formation of real eruption with the ejection of plasma into the interplanetary space [59]. However, due to numerical diffusion — inevitable in difference schemes applied in numerical calculations that are used to simulate mass ejections — field lines can reconnect, even in ideal MHD numerical simulations.

7. Indicators of pre-eruptive states in the solar atmosphere and approaches to forecast mass ejections

No explicit signatures of the 'nascence' of CMEs, their precursors, have been found yet. In analyzing the circumstances under which a mass ejection occurred, it is not infrequent that small-scale changes in photospheric fields are detected in the area from which it had developed; these changes consist in the emergence of new magnetic elements [242, 243] or mutual approach and annihilation ('cancelation') of minor elements of opposite polarity [242–246]. Such changes are also observed, however, in other periods of time and other places. Although these processes may facilitate eruption, they can hardly be regarded as their explicit precursors.

Because, as was noted in Section 5, the free magnetic energy needed to accelerate ejected matter must be accumulated in the corona, it might be reasonable to attempt to find signatures of its presence and track their changes until an eruption occurs. An indicator of the current component of the coronal magnetic field is shear, a deviation of the coronal

loop projection onto the Sun's surface from perpendicularity to PILs. Shear is manifested in the most prominent way in the filament channels where some chromospheric fibrils and threads that constitute the fine structure of filaments can be aligned along PILs. However, the shear in filament channels can be related to the presence of a magnetic flux rope in the corona. Due to equilibrium conditions in the almost potential enveloping field, the rope axis is oriented along the PIL, and its own field lines in the central part are parallel to the axis.

Among the manifestations of magnetic flux ropes in the corona, there are coronal cavities, round or oval-shaped dimmed areas in the base of large coronal rays (streamers) extending above prominences and visible in corona images in the white light and extreme UV range (Fig. 8). The dimmed brightness in white light is an unambiguous indicator of reduced density. It is sometimes interpreted as evidence of a stronger magnetic field being present in the cavity due to magnetohydrostatic conditions. However, if the plasma β parameter is small, which is typically the case in the solar corona, gas pressure is not expected to play a significant role in the distribution of matter. The coronal cavities indeed look like long cylindrical structures elongated along PILs. A cavity is only distinguishable if the line of sight is directed along its axis; otherwise, surrounding bright coronal loops occlude the cavity. Due to the low density, it is usually impossible to discern any internal structure of the cavity. The lower part of a cavity always contains a prominence, a structure that is two orders of magnitude denser and cooler than the enveloping coronal plasma.

The shape of prominences and filaments is usually not similar to the structure of a twisted flux rope. The reason is that dense plasma is accumulated in the lower parts of helical field lines that act as magnetic gravitational traps (Fig. 9). Because only the lower parts of helical lines are seen in the top view projected onto the solar disk, the right-handed helix (Fig. 9c) should contain a filament whose threads deviate from the axis in a clockwise direction (Fig. 9a). If the filament is activated, plasma starts moving along the flux tubes and can 'overflow' across the upper parts, thus revealing the helix structure of the flux rope (Fig. 9b) [176, 207–209, 247].

Structures are observed in the X-ray corona that outline the magnetic configuration where a mass ejection frequently occurs. These are so-called sigmoids, sets of X-ray coronal loops shaped like the letter S or its mirror image (Fig. 10) [248–250]. The central part of a sigmoid is elongated along a PIL, and its ends are bent towards the regions where fields of opposite sign concentrate. It is usually not possible to distinguish a single S-shaped loop that would extend from one end of the sigmoid to the other. The structure is outlined by shorter loops and consists, as it were, of two crescent halves. The loops contain the hot plasma clearly visible in the soft X-ray range and less visible in UV lines.

A structure like this is interpreted as an indicator of strong nonpotentiality and hence large amounts of free magnetic energy (energy of coronal currents) that can be released in an eruptive process. Although S-shaped field lines can also exist in a potential field, calculations of a nonlinear force-free field in the corona based on measured distributions of all three components in the photosphere typically confirm that such areas contain magnetic flux ropes with a wiggling axis (Fig. 10b) [250, 251]. Active regions with the sigmoid structure tend to create CMEs in the wake of which the magnetic configuration's simplified to a simple arcade of loops or a cusped structure [252]. Some sigmoids are created

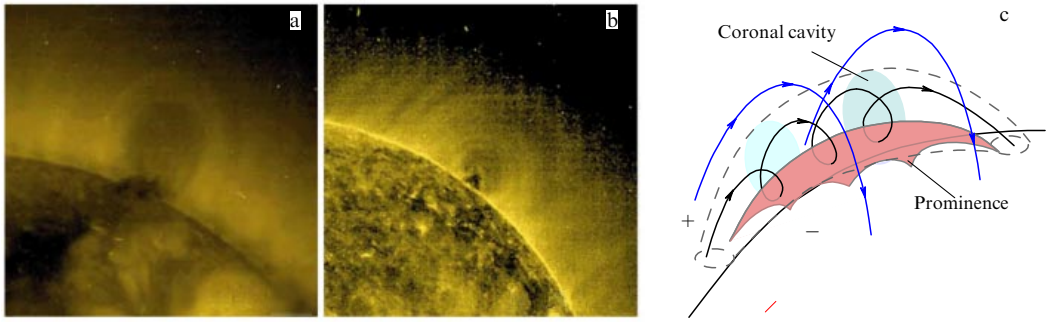

Figure 8. (Color online.) (a, b) Coronal cavities in images taken by the SOHO EIT telescope in the Fe XV 284-Å channel. (c) Schematic rendering of a magnetic flux rope in the corona.

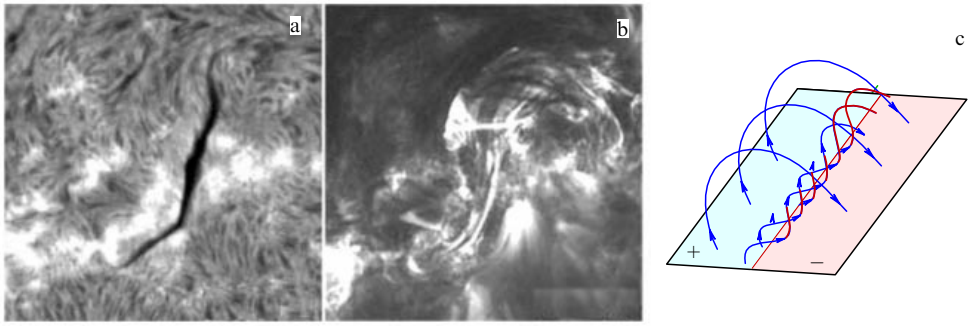

Figure 9. (Color online.) Changes in the filament shape during activation (August1, 2001). (a) Hα filtergram taken at 15:35 UT (Big Bear Solar Observatory). (b) Image of the same area at 18:51 UT in the 171 Å channel of the TRACE orbital telescope. (c) Field lines of the magnetic flux rope that contain filament plasma in the lower parts (red thicker segments).

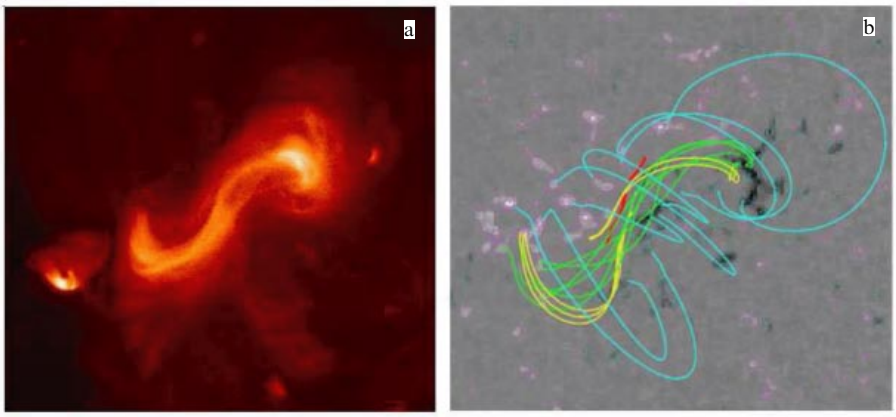

Figure 10. (a) Sigmoid in an image taken by the XRT telescope aboard the Hinode satellite at 06:41 UT on February 12, 2007. (b) Field lines of the nonlinear force-free field calculated using a photospheric magnetogram [250].

as a result of rotation of solar spots that drag magnetic field lines in the corona [253]. The twisted flux rope can then experience magnetic field kink instability when the twist attains a critical value and an eruptive process is initiated.

While it is rather difficult or entirely impossible to estimate the twist of field lines in the flux rope because its structure is only visible in images during activation, prominences enable an easy assessment of the rope axis height above the photosphere. They at least provide a lower estimate for the height, because in the quiescent state the prominence matter is concentrated in the lower parts of helical flux tubes (see Fig. 9), below the flux rope axis. If the magnetic field in the photosphere has also been measured below the prominence, the height at which field decay exponent (14) attains the critical value can be calculated and compared with the actual height of the flux rope. A potential approximation of the magnetic field in the corona is suitable for this calculation, because it is the sources located beneath the photosphere that create the field confining the flux rope in the corona. An analysis like this shows that the height of quiescent prominences is always below the critical value, while the height of the prominences that tend to erupt is close to the instability threshold (Fig. 11) [228, 254]. Detailed tracking of changes in the height of the prominence before eruption (Fig. 12) confirms that the prominence remains quiescent until its height is less than the critical value and comes close to the threshold several hours prior to the eruption [255]. Thus, the ratio of the prominence height to the critical height is a parameter that characterizes the closeness of the magnetic flux rope to the instability threshold and can be used as an instrument to forecast eruptive events on the Sun.

The problem is that data are needed about the height of the prominence and the photospheric magnetic field that refer to the same moment of time. If observations are made from the same point (on Earth's surface or a near-Earth orbit), the conditions favorable for measuring each of these quantities are incompatible. The prominence height can be easily measured when it is located on the Sun's limb or close to it. The line of sight is at this time tangent to the photosphere below it, and the magnetic field cannot be measured. For measurements of the magnetic field to be reliable, the normal to the surface must be directed along the line of sight. Ideally, a spacecraft is needed that would observe the Sun in the direction perpendicular to the Sun–Earth line. This option has been provided by two STEREO space observatories moving in opposite directions in Earth's orbit when they

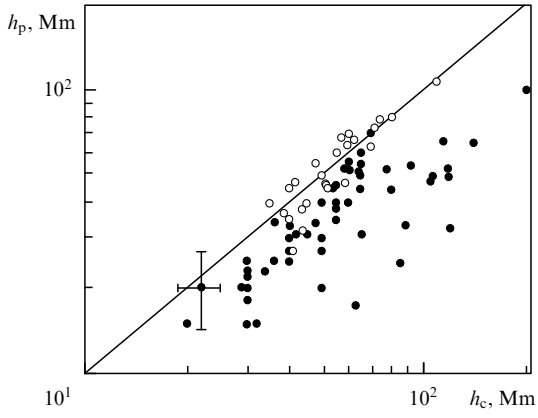

Figure 11. Relation between the limit height of the stable equilibrium of magnetic flux ropes, h_c, and the observed height of prominences above the limb, h_p. The straight line that corresponds to these parameters being equal is the stability boundary. Open circles represent eruptive filaments.

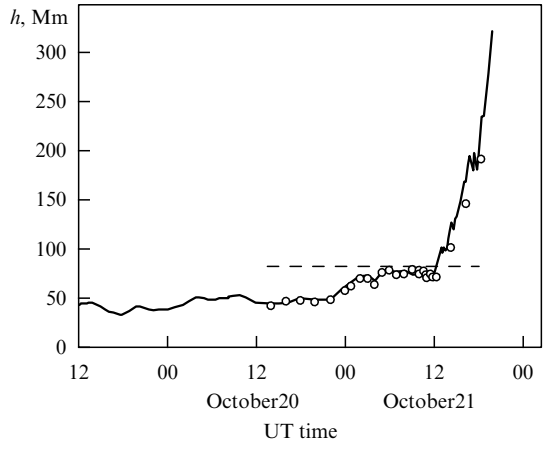

Figure 12. Height of the upper edge of a prominence above the photosphere as a function of time (October 19–21, 2010). The solid line corresponds to data from STEREO A/SECCHI EUVI 304 Å, and circles show the STEREO A/SECCHI EUVI 304 Å data. The dashed line shows the critical height of 80 Mm.

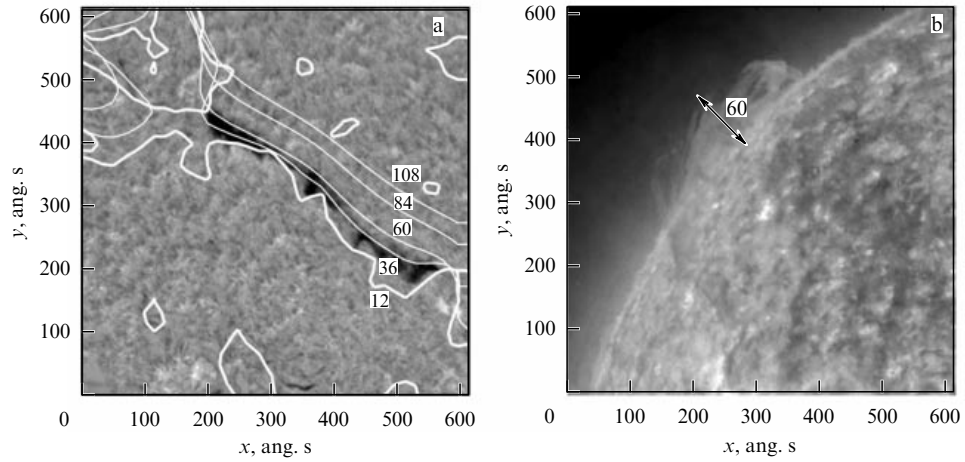

Figure 13. (a) PILs superimposed on an Hα filtergram of the Sun's disk (July1, 2010). (b) The same filament seen on the limb as a prominence at the same time (16 UT) by the STEREO A spacecraft. The numbers show the height expressed in Mm.

attained an angular distance of ±90°. However, the two observatories remained close to this favorable position for only about a year, then moved far away from the required points as they kept moving along the orbit.

Estimates of the eruptive stability of prominences can be derived with some accuracy based on observations made from the same point. It can be assumed for very quiescent prominence that its height does not significantly change during its motion from the limb to the central meridian (about a week) owing to the rotation of the Sun. The height of some prominences can be estimated when they are seen on the disk as filaments, using a kind of a pseudo-stereoscopic effect created by the Sun's rotation. Quiescent prominences often have the form of a curtain or a thin ribbon set on an edge. As a result of the Sun's rotation, the visible width of the ribbon for filaments elongated in the meridional direction significantly changes when the filament passes across the visible disk. These changes can be used to calculate the vertical extension of the prominence.

The width of the filament is minimal for some position on the disk, which is evidence that matter is primarily concentrated near an almost flat surface, and the line of sight is tangential to this surface at this moment. A comparison with the results calculated for the potential field in the corona has shown that this surface almost coincides with the neutral surface of the field $B_r = 0$ [256, 257]. Each PIL calculated for a specific height is a line where the neutral surface is crossed by a horizontal plane. If a set of PILs is computed for various heights and projected onto the image of a filament, the filament matter turns out to be distributed between the lowest PIL located close to the chromosphere and the PIL that corresponds to the height of the upper edge of the filament (Fig. 13). This line, which touches the filament 'spine', determines its height. A comparison with observational data for the same filaments on the limb seen as prominences, which were obtained by the STEREO observatories during the favorable period when they were located away from the Sun–Earth line, shows that this method provides rather good accuracy [258].

Space weather cannot be forecast for a time period exceeding 3 to 4 days without monitoring the state of solar active areas and filaments and assessing probabilities of the development of catastrophic processes with the formation of mass ejections. To estimate the time that the perturbation needs to reach vicinities of Earth, the direction of its motion, its velocity, and the way the mass ejection expands must be known. Perturbation geoeffectiveness depends on the magnitude and direction of the magnetic field it contains. The direction of the axial component of the field in the magnetic flux rope can be determined with some accuracy based on the field structure in the area of the Sun from which it was ejected.

8. Conclusion

Coronal mass ejections are the largest-scale eruptive phenomenon in the solar system. Their drastic effect on space weather is a reason for the significant interest in observing, simulating, and forecasting these events. Various models target various stages and aspects of mass ejections. Some models describe the initial state of areas of the solar atmosphere where the mass ejections are generated. They are used to examine plasma equilibrium in the magnetic field of the corona and ways for instabilities leading to catastrophic processes to develop. Other models are employed to interpret dynamic and kinematic characteristics of the mass ejections observed in the coronagraph field of view. Still other models are used to analyze the propagation of mass ejections from the Sun to Earth and, further, the structure of their magnetic field in interplanetary space, interaction with the solar wind, and changes in shape and volume.

The global shape of the interplanetary magnetic field and the extent to which field lines are twisted in it determine the effective free path of relativistic charged particles on their way from the Sun to Earth and hence the time of their delay in comparison to the time of flight along the Parker spiral of the interplanetary magnetic field. The flux of galactic cosmic rays detected on Earth's surface depends on the shape and strength of the magnetic cloud and shock wave that is related to the cloud. A reduction in this flux is due to deviation and scattering of fast particles by the enhanced magnetic field of the cloud and turbulence in the wake of the shock-wave edge.

Demand for space weather forecasting is growing in all areas of human activities. For a forecast of a geophysical situation to be reliable, primarily, data about active processes on the Sun are needed. Because the time during which the

magnetic cloud ejected from the Sun reaches Earth is rather long (1–4 days), a short-time forecast of space weather is quite reliable if high-quality observational data for the solar corona are available (preferably obtained at various angles, as in the STEREO project). To provide a long-time forecast, it is necessary to be able to estimate the probability of development of sporadic eruptive processes on the Sun.

The catastrophic process of the loss of equilibrium of a large-scale system of currents in the corona is the most probable ejection mechanism. A twisted magnetic flux rope remains confined by the strain of field lines of photospheric sources until parameters of the system reach critical values and the equilibrium becomes unstable. Unfortunately, the major part of the flux rope volume contains low-density plasma (coronal cavity), as a result of which it can only be observed with great difficulty. However, the lower parts of spiral field lines are perfect traps for the dense cold plasma of prominences and hence are the best tracers of magnetic flux ropes in the corona. Some observable characteristics of filaments can be used to assess prospects for the further evolution of the flux rope in the corona.

For studies of the generation and development of CMEs to advance further, more accurate and detailed data are needed about the magnetic configurations in which they are generated, the instability types that trigger eruption, and the role of magnetic reconnection in the process of overcoming the effect of the confining magnetic field and accompanying events. Important new data about processes in the solar corona will come from observations of areas that were previously inaccessible using new instruments. ASPIICS, the European Space Agency's coronagraph [259], will enable observation of the lowest corona layers where matter starts accelerating, and the structure of mass ejections is formed. The Solar Orbiter, an ESA/NASAs project [260], and Intergelioprobe, the Russian Space Agency's project [261], will provide observational data on the Sun from viewpoints located above the ecliptic plane, where spacecraft with telescopes aboard have never orbited before.

It is of importance to reliably establish the initial magnetic configuration type in areas where CMEs are generated, clarify the criteria of stability of the structures that accumulate free magnetic energy, and determine triggers for the development of instabilities. Of great importance for assessing the geoeffectiveness of mass ejections is the forecast of their velocity and direction of propagation. Progress in this area may be attained as a result of studying interaction between CMEs and the ambient magnetic field. Although the magnetic field in the corona remains virtually inaccessible to direct measurements, first, some optimism is inspired by attempts to detect it using various methods, and, second, extrapolation of photospheric data using various approximations (ranging from the condition of field potentiality to models of a nonlinear force-free field or models where the requirement of MHD stability is fulfilled) may be a nice instrument for assessing the evolution of mass ejections.

Some parameters of interplanetary magnetic clouds approaching Earth can be estimated based on the analysis of physical conditions in the area of the Sun where it originated and changes that occurred in that area after the onset of the eruption. However, the evolution of a CME in the heliosphere is affected by factors that depend on the properties of the solar wind along its propagation path.

The author is grateful to the referee for the helpful comments. The author thanks the Big Bear Solar Observatory, New Jersey Institute of Technology, the SOHO, STEREO, Hinode, TRACE, and SDO scientific teams for the high-quality data they supply. SOHO is a project of international cooperation between the ESA and NASA. STEREO is the third mission in NASA's Solar Terrestrial Probes program. SDO is a mission of NASA's Living With a Star Program.

References

1. Willson R C, Mordinov A V *Geophys. Res. Lett.* **30** 1199 (2003)
2. Lilensten J et al. *Ann. Geophys.* **26** 269 (2008)
3. Lukianova R, Mursula K *J. Atmos. Sol.-Terr. Phys.* **73** 235 (2011)
4. Hathaway D H *Living Rev. Solar Phys.* **12** 4 (2015)
5. Ben A O *Living Rev. Solar Phys.* **5** 1 (2008)
6. Carrington R C *Mon. Not. R. Astron. Soc.* **20** 13 (1859)
7. Hodgson R *Mon. Not. R. Astron. Soc.* **20** 15 (1859)
8. Parker E N *Astrophys. J.* **128** 664 (1958)
9. Biermann L *Z. Astrophys.* **29** 274 (1951)
10. Gringauz K I et al. *Sov. Phys. Dokl.* **5** 361 (1960); *Dokl. Akad. Nauk SSSR* **131** 1301 (1960)
11. Neugebauer M, Snyder C W *Science* **138** 1095 (1962)
12. Lio B *C.R. Acad. Sci. Paris* **193** 1169 (1931)
13. Koutchmy S *Space Sci. Rev.* **47** 95 (1988)
14. DeForest C E, Howard T A, McComas D J *Astrophys. J.* **769** 43 (2013)
15. Zhao X P, Webb D F *J. Geophys. Res.* **108** 1234 (2003)
16. Zurbuchen T H, Richardson I G *Space Sci. Rev.* **123** 31 (2006)
17. Lepping R P, Jones J A, Burlaga L F *J. Geophys. Res.* **95** 11957 (1990)
18. Chi Y et al. *Solar Phys.* **291** 2419 (2016)
19. Gosling J T *J. Geophys. Res.* **98** 18937 (1993)
20. Kunow H et al. (Eds) *Coronal Mass Ejections* (Space Sciences Ser. of ISSI, Vol. 21) (Dordrecht: Springer, 2006)
21. Filippov B P *Eruptivnye Protsessy na Solntse* (Eruptive Processes in the Sun) (Moscow: Fizmatlit, 2007)
22. Chen P F *Living Rev. Solar Phys.* **8** 1 (2011)
23. Howard T *Coronal Mass Ejections. An Introduction* (Astrophysics Space Sciences Library, Vol. 376) (New York: Springer, 2011)
24. Webb D F, Howard R A *Living Rev. Solar Phys.* **9** 3 (2012)
25. Schmieder B, Aulanier G, Vršnak B *Solar Phys.* **290** 3457 (2015)
26. Chen J *Phys. Plasmas* **24** 090501 (2017)
27. Brueckner G E et al. *Solar Phys.* **162** 357 (1995)
28. Howard R A et al. *Space Sci. Rev.* **136** 67 (2008)
29. Eyles C J et al. *Solar Phys.* **254** 387 (2009)
30. Eyles C J et al. *Solar Phys.* **217** 319 (2003)
31. Hou J, de Wijn A, Tomczyk S *Astrophys. J.* **774** 85 (2013)
32. Nakajima H et al. *Proc. IEEE* **82** 705 (1994)
33. Paetzold et al. *Solar Phys.* **279** 127 (2012)
34. Koutchmy S, Stellmacher G *Solar Phys.* **49** 253 (1976)
35. Rompolt B, Švestka Z *Adv. Space Res.* **17** 115 (1996)
36. Sterling A C *Solar Phys.* **196** 79 (2000)
37. Yamauchi Y et al. *Astrophys. J.* **629** 572 (2005)
38. Liu Y *Solar Phys.* **249** 75 (2008)
39. Schmieder B, in *Dynamics and Structure of Quiescent Solar Prominences* (Ed. E R Priest) (Dordrecht: Kluwer Acad. Publ., 1989) p. 15
40. Babcock H W, Babcock H D *Astrophys. J.* **121** 349 (1955)
41. Howard R F, Harvey J W *Astrophys. J.* **139** 1328 (1964)
42. Smith S F, Ramsey H E *Solar Phys.* **2** 158 (1967)
43. McIntosh P S *Rev. Geophys. Space Phys.* **10** 837 (1972)
44. Snodgrass H B, Kress J M, Wilson P R *Solar Phys.* **191** 1 (2000)
45. Durrant C J *Solar Phys.* **211** 83 (2002)
46. Zirin H, in *Physics of Solar Prominences, Proc. of the Intern. Astronomical Union, Colloquium No. 44, Oslo, August 14–18, 1978* (Eds E Jensen, P Maltby, F Q Orrall) (Oslo: Univ. of Oslo, Inst. of Theoretical Astrophysics, 1979) p. 193
47. Vrsnak B, Ruzdjak V, Rompolt B *Solar Phys.* **136** 151 (1991)
48. Nakagawa Y, Wu S T, Tandberg-Hanssen E *Solar Phys.* **41** 387 (1975)
49. Tang F *Solar Phys.* **107** 233 (1986)
50. Cheng X, Kliem B, Ding M D *Astrophys. J.* **856** 48 (2018); arXiv:1802.04932

51. Gopalswamy N et al. *Earth Moon Planets* **104** 295 (2009)
52. Robbrecht E, Berghmans D *Astron. Astrophys.* **425** 1097 (2004)
53. Robbrecht E, Berghmans D, van der Linden R A M *Astrophys. J.* **691** 1222 (2009)
54. Boursier Y et al. *Solar Phys.* **257** 125 (2009)
55. Floyd O et al. *Solar Phys.* **288** 269 (2013)
56. Olmedo O et al. *Solar Phys.* **248** 485 (2008)
57. Gopalswamy N et al., in *Magnetic Coupling Between the Interior and the Atmosphere of the Sun* (Eds S S Hasan, R J Rutten) (Berlin: Springer, 2010) p. 289
58. Robbrecht E, Patsourakos S, Vourlidas A *Astrophys. J.* **701** 283 (2009)
59. Forbes T G *J. Geophys. Res.* **105** 23153 (2000)
60. Gopalswamy N, in *The Sun and the Heliosphere as an Integrated System* (Eds Poletto G, Suess S T) (Astrophysics and Space Science Library, Vol. 317) (Dordrecht: Kluwer Acad. Publ., 2004) p. 201
61. Vourlidas A et al. *Astrophys. J.* **722** 1522 (2010)
62. Xue X H, Wang C B, Dou X K *J. Geophys. Res.* **110** A08103 (2005)
63. Michalek G et al. *Astron. Astrophys.* **423** 729 (2004)
64. Veselovsky I S, Panasenko O A *Solar Syst. Res.* **39** 421 (2005); *Astron. Vestn.* **39** 469 (2005)
65. Wu C-C, Lepping R P *Solar Phys.* **269** 141 (2011)
66. Richardson I G, Cane H V *Solar Phys.* **264** 189 (2010)
67. Dasso S et al. *Solar Phys.* **244** 115 (2007)
68. Lundquist S *Phys. Rev.* **83** 307 (1951)
69. Démoulin P, Dasso S *Astron. Astrophys.* **507** 969 (2009)
70. Hu Q, Qiu J, in *Nature of Prominences and Their Role in Space Weather, Proc. IAU Symp. 300* (Eds B Schmieder, J-M Malherbe, S T Wu) (Cambridge: Cambridge Univ. Press, 2013) p. 269
71. Nieves-Chinchilla T et al. *Astrophys. J.* **823** 27 (2016)
72. Hu Q, Sonnerup B U O *J. Geophys. Res.* **107** 1142 (2002)
73. Nakwacki M et al. *J. Atm. Solar-Terr. Phys.* **70** 1318 (2008)
74. Démoulin P et al. *Solar Phys.* **250** 347 (2008)
75. Gulisano A M et al. *Astron. Astrophys.* **509** A39 (2010)
76. Nakwacki M et al. *Astron. Astrophys.* **535** A52 (2011)
77. Lin J et al. *Astrophys. J.* **504** 1006 (1998)
78. Romashets E P, Vandas M *J. Geophys. Res.* **106** 10615 (2001)
79. Farrugia C J, Osherovich V A, Burlaga L F *J. Geophys. Res.* **100** 12293 (1995)
80. Grechnev V V et al. *Solar Phys.* **289** 4653 (2014)
81. Cargill P J, Schmidt J M *Ann. Geophys.* **20** 879 (2002)
82. Lugaz N, Roussev I *J. Atm. Solar Terr. Phys.* **73** 1187 (2011)
83. Vandas M et al. *J. Geophys. Res.* **102** 24183 (1997)
84. Webb D F, Krieger A S, Rust D M *Solar Phys.* **48** 159 (1976)
85. Munro R H et al. *Solar Phys.* **61** 201 (1979)
86. Webb D F, Hundhausen A J *Solar Phys.* **108** 383 (1987)
87. St Cyr O C, Webb D F *Solar Phys.* **136** 379 (1991)
88. Gilbert H R et al. *Astrophys. J.* **537** 503 (2000)
89. Ji H et al. *Astrophys. J.* **595** L135 (2003)
90. Török T, Kliem B *Astrophys. J.* **630** L97 (2005)
91. Alexander D, Liu R, Gilbert H R *Astrophys. J.* **653** 719 (2006)
92. Kuridze D et al. *Astron. Astrophys.* **552** A55 (2013)
93. Kushwaha U et al. *Astrophys. J.* **807** 101 (2015)
94. Hori K, Culhane J L *Astron. Astrophys* **382** 666 (2002)
95. Yang G, Wang H, in *Solar-Terrestrial Magnetic Activity and Space Environment* (COSPAR Colloq. Ser., Vol. 14, Eds H Wang, R Xu) (Boston: Pergamon, 2002) p. 113
96. Jing J et al. *Astrophys. J.* **614** 1054 (2004)
97. Gopalswamy N et al. *Astrophys. J.* **586** 562 (2003)
98. Plunkett S P et al. *Adv. Space Res.* **29** 1473 (2002)
99. Gopalswamy N et al. *Adv. Space Res.* **25** 1851 (2000)
100. Lozhechkin A V, Filippov B P *Astron. Rep.* **48** 145 (2004); *Astron. Zh.* **81** 168 (2004)
101. Liewer P et al. *Solar Phys.* **290** 3343 (2015)
102. McCauley P I et al. *Solar Phys.* **290** 1703 (2015)
103. Gopalswamy N, in *Solar Prominences* (Astrophysics Space Sciences Library, Vol. 415, Eds J-C Vial, O Engvold) (Cham: Springer, 2015) p. 381
104. Filippov B P *Astron. Rep.* **60** 356 (2016); *Astron. Zh.* **93** 321 (2016)
105. Steinolfson R S, Nakagawa Y *Astrophys. J.* **215** 345 (1977)
106. Dryer M et al. *Astrophys. J.* **227** 1059 (1979)
107. Webb D F, in *Proc. of the SOHO 11 Symp. on from Solar Min to Max: Half a Solar Cycle with SOHO, 11–15 March 2002, Davos, Switzerland* (ESA SP-508, Ed. A Wilson) (Noordwijk: ESA Publications Division, 2002) p. 409
108. Gopalswamy N, Yashiro S, Akiyama S *J. Geophys. Res.* **112** A06112 (2007)
109. Andrews M D *Solar Phys.* **218** 261 (2003)
110. Yashiro S et al. *J. Geophys. Res.* **110** A12S05 (2005)
111. Wang Y, Zhang J *Astrophys. J.* **665** 1428 (2007)
112. MacQueen R M, Fisher R R *Solar Phys.* **89** 89 (1983)
113. Sheeley N R et al. *J. Geophys. Res.* **104** 24739 (1999)
114. Andrews M D, Howard R A *Space Sci. Rev.* **95** 147 (2001)
115. Moon Y-J et al. *Astrophys. J.* **581** 694 (2002)
116. Zhang J et al. *Astrophys. J.* **559** 452 (2001)
117. Vrsnak B et al. *Solar Phys.* **225** 355 (2004)
118. Zhang J, Dere K P *Astrophys. J.* **649** 1100 (2006)
119. Maricic D et al. *Solar Phys.* **241** 99 (2007)
120. Vourlidas A et al. *Astrophys. J.* **534** 456 (2000)
121. Hudson H S *Solar Phys.* **133** 357 (1990)
122. Parnell C E, Jupp P E *Astrophys. J.* **529** 554 (2000)
123. Harrison R A *Astron. Astrophys.* **304** 585 (1995)
124. Hundhausen A J, in *The Many Faces of the Sun: a Summary of the Results from NASA's Solar Maximum Mission* (Eds K T Strong et al.) (New York: Springer, 1999) p. 143
125. Schmieder B et al. *Solar Phys.* **156** 337 (1995)
126. Warren H P, O'Brien C M, Sheeley N R (Jr.) *Astrophys. J.* **742** 92 (2011)
127. Tripathi D, Bothmer V, Cremades H *Astron. Astrophys.* **422** 337 (2004)
128. Rust D M, Hildner E *Solar Phys.* **48** 381 (1976)
129. Sterling A C, Hudson H S *Astrophys. J.* **491** L55 (1997)
130. Thompson B J et al. *Geophys. Res. Lett.* **25** 2465 (1998)
131. Thompson B J et al. *Geophys. Res. Lett.* **27** 1431 (2000)
132. Jiang Y et al. *Astrophys. J.* **597** L161 (2003)
133. McIntosh S W et al. *Astrophys. J.* **660** 1653 (2007)
134. Thompson B J et al. *Geophys. Res. Lett.* **25** 2461 (1998)
135. Harrison R A, Lyons M *Astron. Astrophys.* **358** 1097 (2000)
136. Gopalswamy N, Thompson B J *J. Atm. Solar-Terr. Phys.* **62** 1457 (2000)
137. Zarro D M et al. *Astrophys. J.* **520** L139 (1999)
138. Harra L K, Sterling A C *Astrophys. J.* **561** L215 (2001)
139. Harrison R A et al. *Astron. Astrophys.* **400** 1071 (2003)
140. Rust D M *Space Sci. Rev.* **34** 21 (1983)
141. Qiu J, Yurchyshyn V B *Astrophys. J.* **634** L121 (2005)
142. Qiu J et al. *Astrophys. J.* **659** 758 (2007)
143. Chertok I M et al. *Solar Phys.* **282** 175 (2013)
144. Chertok I M, Grechnev V V, Abunin A A *Solar Phys.* **292** 62 (2017)
145. Biesecker D A et al. *Astrophys. J.* **569** 1009 (2002)
146. Thompson B J, Myers D C *Astrophys. J. Suppl.* **183** 225 (2009)
147. Hudson H S et al. *Solar Phys.* **212** 121 (2003)
148. Mancuso S, Raymond J C *Astron. Astrophys.* **413** 363 (2004)
149. Vourlidas A et al. *Astrophys. J.* **598** 1392 (2003)
150. Ontiveros V, Vourlidas A *Astrophys. J.* **693** 267 (2009)
151. Eselevich V G, Eselevich M V *Astron. Rep.* **58** 260 (2014); *Astron. Zh.* **91** 320 (2014)
152. Gosling J T et al. *Solar Phys.* **40** 439 (1975)
153. McComas D J et al. *J. Geophys. Res.* **103** 1955 (1998)
154. Kahler S W, Hildner E, van Hollebeke M A I *Solar Phys.* **57** 429 (1978)
155. Tylka A J. *Geophys. Res.* **106** 25233 (2001)
156. Gopalswamy N et al. *Ann. Geophys.* **26** 1 (2008)
157. Dodson H W, Hedeman E R *Planet. Space Sci.* **12** 393 (1964)
158. Howard T A, Harrison R A *Solar Phys.* **285** 269 (2013)
159. D'Huys E et al. *Astrophys. J.* **795** 49 (2014)
160. Nitta N V, Mulligan T *Solar Phys.* **292** 125 (2017)
161. Chen J *Astrophys. J.* **338** 453 (1989)
162. Antiochos S K, Dahlburg R B, Klimchuk J A *Astrophys. J.* **420** L41 (1994)
163. Aulanier G, DeVore C R, Antiochos S K *Astrophys. J.* **567** L97 (2002)
164. Aly J J *Astron. Astrophys.* **143** 19 (1985)
165. Aly J J *Astrophys. J.* **283** 349 (1984)
166. Aly J J *Astrophys. J.* **375** L61 (1991)
167. Sturrock P A *Astrophys. J.* **380** 655 (1991)

168. Antiochos S K, DeVore C R, Klimchuk J A *Astrophys. J.* **510** 485 (1999)
169. Lynch B J et al. *Astrophys. J.* **683** 1192 (2008)
170. Lynch B J, Edmondson J K *Astrophys. J.* **784** 87 (2013)
171. Syrovatskii S I *Solar Phys.* **76** 3 (1982)
172. Archontis V, Torok T *Astron. Astrophys.* **492** L35 (2008)
173. MacTaggart D, Hood A W *Astron. Astrophys.* **508** 445 (2009)
174. DeVore C R, Antiochos S K *Astrophys. J.* **539** 954 (2000)
175. Aulanier G et al. *Astrophys. J.* **708** 314 (2010)
176. Joshi N C et al. *Astrophys. J.* **787** 11 (2014)
177. James A W et al. *Solar Phys.* **292** 71 (2017)
178. van Ballegooijen A A, Martens P C H *Astrophys. J.* **343** 971 (1989)
179. Green L M, Kliem B, Wallace A J *Astron. Astrophys.* **526** A2 (2011)
180. Amari T et al. *Astrophys. J. Lett.* **529** L49 (2000)
181. Xia C, Keppens R, Guo Y *Astrophys. J.* **780** 130 (2014)
182. Mackay D H, van Ballegooijen A A *Astrophys. J.* **641** 577 (2006)
183. Yeates A R, Mackay D H *Astrophys. J.* **699** 1024 (2009)
184. Parker E N *Cosmical Magnetic Fields. Their Origin and Their Activity* (Oxford: Clarendon Press, 1979)
185. Fan Y *Astrophys. J.* **554** L111 (2001)
186. Manchester IV W et al. *Astrophys. J.* **610** 588 (2004)
187. Magara T *Astrophys. J.* **748** 53 (2011)
188. Okamoto T J et al. *Astrophys. J.* **673** L215 (2008)
189. Okamoto T J et al. *Astrophys. J.* **697** 913 (2009)
190. Lites B W et al. *Astrophys. J.* **718** 474 (2010)
191. Ballester J L *Solar Phys.* **94** 151 (1984)
192. Kulikova G N et al. *Solnechnye Dannye* (10) 60 (1986)
193. Vrsnak B et al. *Solar Phys.* **116** 45 (1988)
194. Srivastava N, Ambastha A, Bhatnagar A *Solar Phys.* **133** 339 (1991)
195. Filippov B et al. *J. Astrophys. Astron.* **36** 157 (2015)
196. Longcope D W, Welsch B T *Astrophys. J.* **545** 1089 (2000)
197. Török T et al. *Astrophys. J. Lett.* **782** L10 (2014)
198. Izenberg P A, Forbes T G, Démoulin P *Astrophys. J.* **417** 368 (1993)
199. Kadomtsev B B, in *Reviews of Plasma Physics* Vol. 2 (Ed. M A Leontovich) (New York: Consultants Bureau, 1966); Translated into Russian: *Voprosy Teorii Plazmy* Iss. 2 (Ed. M A Leontovich) (Moscow: Gosatomizdat, 1963) p. 132
200. Gold T, Hoyle F *Mon. Not. R. Astron. Soc.* **120** 89 (1960)
201. Hood A W, Priest E R *Solar Phys.* **64** 303 (1979)
202. Fan Y, Gibson S E *Astrophys. J.* **589** L105 (2003)
203. Fan Y, Gibson S E *Astrophys. J.* **609** 1123 (2004)
204. Kliem B, Titov V S, Török T *Astron. Astrophys.* **413** L23 (2004)
205. Török T, Kliem B *Astron. Astrophys.* **406** 1043 (2003)
206. Török T, Kliem B, Titov V S *Astron. Astrophys.* **413** L27 (2004)
207. Filippov B P *Astron. Rep.* **55** 541 (2011); *Astron. Zh.* **88** 587 (2011)
208. Yang L et al. *Astrophys. J. Lett.* **784** L36 (2014)
209. Wang H et al. *Nature Commun.* **6** 7008 (2015)
210. Srivastava A K et al. *Astrophys. J.* **715** 292 (2010)
211. Kumar P et al. *Solar Phys.* **266** 39 (2010)
212. Li T, Zhang J *Solar Phys.* **290** 2857 (2015)
213. Gary G A, Moore R L *Astrophys. J.* **611** 545 (2004)
214. Liu Y et al. *Astrophys. J.* **593** L137 (2003)
215. Régnier S, Amari T *Astron. Astrophys.* **425** 345 (2004)
216. Bobra M G, van Ballegooijen A A, DeLuca E E *Astrophys. J.* **672** 1209 (2008)
217. Canou A et al. *Astrophys. J. Lett.* **693** L27 (2009)
218. Jing J et al. *Astrophys. J. Lett.* **719** L56 (2010)
219. Su Y et al. *Astrophys. J.* **734** 53 (2011)
220. Guo Y et al. *Astrophys. J.* **779** 157 (2013)
221. Sakurai T *Publ. Astron. Soc. Jpn.* **28** 177 (1976)
222. Fan Y, Gibson S E *Astrophys. J.* **668** 1232 (2007)
223. van Tend W, Kuperus M *Solar Phys.* **59** 115 (1978)
224. Molodenskii M M, Filippov B P *Sov. Astron.* **31** 564 (1987); *Astron. Zh.* **64** 1079 (1987)
225. Martens P C H, Kuin N P M *Solar Phys.* **122** 263 (1989)
226. Priest E R, Forbes T G *Solar Phys.* **126** 319 (1990)
227. Filippov B P, Den O G *Astron. Lett.* **26** 322 (2000); *Pis'ma Astron. Zh.* **26** 322 (2000)
228. Filippov B P, Den O G *J. Geophys. Res.* **106** 25177 (2001)
229. Forbes T G, Isenberg P A *Astrophys. J.* **373** 294 (1991)
230. Forbes T G, Priest E R *Astrophys. J.* **446** 377 (1995)
231. Lin J, Forbes T G *J. Geophys. Res.* **105** 2375 (2000)
232. Lin J, van Ballegooijen A A *Astrophys. J.* **576** 485 (2002)
233. Schmieder B, Démoulin P, Aulanier G *Adv. Space Res.* **51** 1967 (2013)
234. Longcope D W, Forbes T G *Solar Phys.* **289** 2091 (2014)
235. Shafranov V D, in *Reviews of Plasma Physics* Vol. 2 (Ed. M A Leontovich) (New York: Consultants Bureau, 1966) p. 103; Translated into Russian: in *Voprosy Teorii Plazmy* Iss. 2 (Ed. M A Leontovich) (Moscow: Gosatomizdat, 1963) p. 92
236. Osovets S M, in *Fizika Plazmy i Problema Upravlyaemykh Termoyadernykh Reaktsii* (Plasma Physics and Controlled Thermonuclear Reactions) (Ed. M A Leontovich) (Moscow: Izd. Akad. Nauk SSSR, 1958) p. 238
237. Bateman G *MHD Instabilities* (Cambridge: The Massachusetts Institute of Technology, 1978)
238. Kliem B, Török T *Phys. Rev. Lett.* **96** 255002 (2006)
239. Démoulin P, Aulanier G *Astrophys. J.* **718** 1388 (2010)
240. Kliem B et al. *Astrophys. J.* **789** 46 (2014)
241. Moore R L et al. *Astrophys. J.* **552** 833 (2001)
242. Feynman J, Martin S F *J. Geophys. Res.* **100** 3355 (1995)
243. Gopalswamy N et al. *Space Sci. Rev.* **123** 303 (2006)
244. Martin S F, Livi S H B, in *Eruptive Solar Flares, Proc. IAU Coll., No. 133* (Lecture Notes in Physics, Vol. 399, Eds Z Svestka, B V Jackson, M E Machado M E) (Berlin: Springer, 1992) p. 33
245. Gaizauskas V *Adv. Space Res.* **13** 5 (1993)
246. Lin J, Raymond J C, van Ballegooijen A A *Astrophys. J.* **602** 422 (2004)
247. Filippov B P *Astron. Rep.* **61** 891 (2017); *Astron. Zh.* **94** 883 (2017)
248. Rust D M, Kumar A *Astrophys. J.* **464** L199 (1996)
249. Canfield R C, Hudson H S, McKenzie D E *Geophys. Res. Lett.* **26** 627 (1999)
250. Savcheva A et al. *Astrophys. J.* **750** 15 (2012)
251. Joshi N C et al. *Astrophys. J.* **812** 50 (2015)
252. Sterling A C et al. *Astrophys. J.* **532** 628 (2000)
253. Nightingale R W et al., American Geophysical Union, Fall Meeting 2001, Abstract No. SH11C-0724
254. Filippov B, Zagnetko A *J. Atmos. Solar-Terr. Phys.* **70** 614 (2008)
255. Filippov B P *Astron. Rep.* **57** 778 (2013); *Astron. Zh.* **90** 848 (2013)
256. Zagnetko A M, Filippov B P, Den O G *Astron. Rep.* **49** 425 (2005); *Astron. Zh.* **82** 474 (2005)
257. Filippov B P *Cosmic Res.* **55** 12 (2017); *Kosmich. Issled.* **55** (1) 14 (2017)
258. Filippov B P *Geomagn. Aeronom.* **56** 1 (2016); *Geomagn. Aeronomiya* **56** (1) 3 (2016)
259. Vivès S et al. *Adv. Space Res.* **43** 1007 (2009)
260. Marsch E et al. *Adv. Space Res.* **36** 1360 (2005)
261. Kuznetsov V D, Zelenyi L M, in *Solnechno-Zemnaya Fizika* (Solar-Terrestrial Physics) Iss. 12 *Trudy Mezhdunarodnogo Simpoziuma "Mezhdunarodnyi Geliofizicheskii God — 2017: Novyi Vzglyad na Solnechno-Zemnuyu Fiziku", Zvenigorod, 5–11 Noyabrya 2017 g.* (Proc. of the Intern. Symp. "International Heliophysical Year — 2017: A New Look at Solar-Terrestrial Physics", Zvenigorod, 5–11 November, 2007) Vol. 1 (Novosibirsk: Izd. SO RAN, 2008) p. 83